# Lattice-Boltzmann modelling of spatial variation in surface tension and wetting effects

## Sigvat Kuekiatngam Stensholt

Department of Mathematics
University of Bergen

May 31, 2010

# Preface

This thesis consists of work done during PhD studies at the University of Bergen from January 2006. The focus of the work has been studying the effects of surface tension variations by using the lattice Boltzmann method.

While I have been employed by the Department of Mathematics at the University of Bergen during the scholarship, much of the work has been conducted in cooperation with the Center of Integrated Petroleum Research (CIPR) at the same faculty. Variations of surface tension have been of interest to CIPR because of the use of surfactants for oil recovery. The purpose of the work has been to study how surface tension is handled by the lattice Boltzmann model, and how reductions to surface tension can be sensibly implemented.

# Outline

The main focus of the project which is the foundation of the thesis is to study the effects spatial variations in capillary effects have on fluid flow. This requires knowledge of the underlying fluid flow equations, and some sort of numerical method to handle numerical simulations.

The first part of this thesis deals with the underlying theory of the methods. Classical fluid theory has a brief introduction, followed by the lattice Boltzmann theory and methods for two phase flow and some basic simulations to demonstrate how the two-phase flow methods work. Papers which have been submitted or presented make up the second part of the thesis.

Chapter 1 in the thesis covers classical fluid flow. A particular emphasis is placed on the capillary effects of surface tension, and wetting. The chapter also covers theory on surfactants and their applications.

Chapter 2 covers the foundations of the lattice Boltzmann method which I used throughout the project. The methods are a fairly new way of simulating fluid flow, even though it is based on the century old Boltzmann equation. The underlying algorithms are simple, but the simulated flow can be quite complex.

Chapter 3 covers how the lattice Boltzmann method deals with more complex flow. This includes multiphase flow and flow with solute components. Variations in surface tension are also covered.

Chapter 4 illustrates some of the properties found in the multiphase lattice Boltzmann methods used in this thesis.

Chapter 5 is a summary of the work conducted. A short description of the papers included in the second part of this thesis is provided. The chapter also considers further extensions and possible improvements to the work in this thesis.

## Acknowledgements

Sigvat K. Stensholt
Bergen, May 2010

# Contents

# Chapter 1

# Fluid theory

## 1.1  Classical equations for single-phase fluid flow

Fluid modelling is the study of fluid movement. In particular, the main concern is finding the fluid's velocity $u$, density $\rho$ and pressure $p$ at different locations $x$.

Classical fluid mechanics involves two fundamental equations; these are given in many textbooks, such as Landau and Lifshitz [1]. The first equation is a direct consequence of the law of mass conservation and given by

$$\frac{\partial \rho}{\partial t} + \nabla \cdot (\rho u) = 0. \tag{1.1}$$

The consequence of the continuity equation is that any net mass flux into an arbitrary volume results in a corresponding increase in density in that volume. If we are dealing with incompressible fluids, $\rho$ is constant, and (1.1) is simplified to

$$\nabla \cdot u = 0. \tag{1.2}$$

The second equation deals with the effects forces have on fluid motion. This includes external forces $F$ such as gravity, and internal forces such as interparticle friction (viscosity). Assuming that the viscous properties are independent of the fluid temperature and pressure, the equation is given by

$$\rho \left( \frac{\partial u}{\partial t} + (u \cdot \nabla)u \right) = -\nabla p + F + \mu \nabla^2 u + (\zeta + \frac{\mu}{3})\nabla(\nabla \cdot u), \tag{1.3}$$

and called the Navier-Stokes equation. The parameters $\mu$ and $\zeta$ are the dynamic and second viscosities of the fluid. For an incompressible fluid, the last term in equation (1.3) vanishes, and we can write

$$\frac{\partial u}{\partial t} + (u \cdot \nabla)u = -\frac{1}{\rho}(\nabla p + F) + \nu \nabla^2 u, \tag{1.4}$$

where $v = \frac{\mu}{\rho}$ is called the kinematic viscosity.

The further simplified Navier-Stokes equation where viscous forces are neglected is called the Euler equation and given by

$$\frac{\partial \boldsymbol{u}}{\partial t} + (\boldsymbol{u} \cdot \nabla)\boldsymbol{u} = -\frac{1}{\rho}(\nabla p + \boldsymbol{F}). \tag{1.5}$$

## 1.2   Surface tension

When two fluids are present, an important distinction must be made between miscible and immiscible fluids. If the fluids are miscible, the molecules of each component can mix together, and form a solution. In contrast, immiscible fluids such as the idiomatic oil and water pairing, cannot mix together and the molecules of each fluid form separate phases.

The pressure across the interface of two phases may be discontinuous due to the presence of an effect called surface tension. The cause of surface tension is that molecules at the interface are subjected to different intermolecular forces than the molecules away from the interface.

In standard modelling, it is common to divide the fluid into "pure" regions where a single component dominates and accounts for all the thermodynamical properties, and interfacial regions where the presence of multiple components causes the thermodynamical properties to change.

### 1.2.1   Molecular origins

Attractive but short-range intermolecular forces (for example, Van der Waals forces, dipole bonds, and hydrogen bonds) exist between the molecules in a liquid. Most particles in a liquid are surrounded by other molecules of the same type, and the attractive forces from different molecules will roughly balance each other. The intermolecular forces give rise to a cohesion energy $U$.

However, these forces are imbalanced for molecules on the surface of the liquid, and as a result the cohesion energy for these particles is on the order of $U/2$. If the surface molecule has an area of $a^2$, the surface tension will be of order $\frac{U}{2}a^2$ [2].

### 1.2.2   Fluid theory of surface tension

For the traditional fluid theory of surface tension, we turn to the variational calculations by Landau and Lifshitz [1].

Assume we have an interface with the fluids "red" (superscript $R$) and "blue" (superscript $B$) on either side. The pressure on the red and sides are $p^R$ and $p^B$

respectively, and the difference in pressure is denoted $\Delta p = p^R - p^B$. We now assume that an area of the interface $dA$ is displaced by a short distance $\delta\xi$ towards the blue phase. Assuming no surface tension forces, the work needed to displace this element is

$$dW = (p^B - p^R)\delta\xi dA. \tag{1.6}$$

Unless $p^B = p^R$, this is non-zero, and the interface would move spontaneously towards the phase with lower pressure. In order to maintain a pressure difference, we account for the work needed to stretch the surface element $dA$ by $\delta$, this is given by $\frac{\sigma}{2}\delta$, where $\sigma$ is a surface tension coefficient.

The work needed to perturb the entire interface $A$ by $d\xi$ is then

$$\Delta W = \int (p^R - p^B)\delta\xi dA - \frac{\sigma}{2}\delta A, \tag{1.7}$$

which needs to be zero in order to have a stable interface.

To determine the change in surface area $\delta A$, we need to find the curvature of the interface. For the three-dimensional case, let the two curvature radii be $r_1$ and $r_2$, and let the unperturbed surface element $dA = dl_1 dl_2$. The surface area after the perturbation is then

$$dA + \delta A = dl_1 \left(1 + \frac{\delta\xi}{r_1}\right) dl_2 \left(1 + \frac{\delta\xi}{r_2}\right) \approx dl_1 dl_2 \left(1 + \frac{\delta\xi}{r_1} + \frac{\delta\xi}{r_2}\right). \tag{1.8}$$

The total change in area $\delta A$ is therefore

$$\delta A = \int \delta\xi \left(\frac{1}{r_1} + \frac{1}{r_2}\right) dA, \tag{1.9}$$

which can be inserted into (1.7) to give

$$\Delta W = \int \delta\xi \left((p^R - p^B) - \frac{\sigma}{2}\left(\frac{1}{r_1} + \frac{1}{r_2}\right)\right) dA. \tag{1.10}$$

Setting (1.10) to zero yields Laplace's equation

$$p^R - p^B = \frac{\sigma}{2}\left(\frac{1}{r_1} + \frac{1}{r_2}\right). \tag{1.11}$$

From (1.11) we can see that only curved interfaces yield any pressure difference. Furthermore, if the pressure in each phase is constant, the requirement

$$\frac{1}{r_1} + \frac{1}{r_2} = \text{constant} \tag{1.12}$$

means that the interface must be spherical if the pressure inside the droplet is constant.

In the case of a spherical droplet, $r_1 = r_2 \equiv r$ and we can write

$$p^R - p^B = \frac{\sigma}{r}. \tag{1.13}$$

## 1.3   Processes in fluids with droplets

In many cases, one of the phases forms droplets inside the other. The situation where there is a large number of very small droplets, and where the large amount of interfaces plays a significant role in determining the fluid properties is called an *emulsion*. The component comprising the droplets makes up the *disperse phase*, while the surrounding component makes up the *continuous phase*. Generally, the volume fraction is larger for the continuous phase than the disperse phase. If the volume fraction of the disperse phase is increased so that it exceeds the volume fraction of the continuous phase, a process called *phase inversion* may occur. As the droplets of the large disperse phase coalesce, they may trap pockets of the continuous phase between them. These trapped pockets from the previously continuous phase form droplets, and become the disperse phase.

Since several small droplets have a much larger surface than a single large droplet, emulsions tend to be unstable. There is a strong tendency for the small droplets to merge together and form larger droplets. There are several processes where this takes place.

*Flocculation* is the aggregation of the disperse droplets caused by attractive van der Waals forces between them. *Coalescence* is the process when droplets fuse together due to the film between them disappearing. *Disproportionation* or *Ostwald Ripening* occurs when the fluids are not entirely immiscible, the smallest droplets may diffuse into the continuous phase and be deposited on larger droplets. In the presence of gravity or other external forces, the particles in the disperse phase may separate from the continuous phase by rising or sinking; these processes are called *creaming* and *sedimentation* [3].

Since the free energy (energy capable of performing work) at the interfaces declines with fewer and larger droplets, so the process is usually spontaneous. In real fluids this is aided by the van der Waals attraction between droplets. Emulsions can often be stabilized through the introduction of emulsifiers, creating energy barriers which prevent the aforementioned processes. Emulsifiers introduce repellent forces which counteract the attractive van der Waals effects.
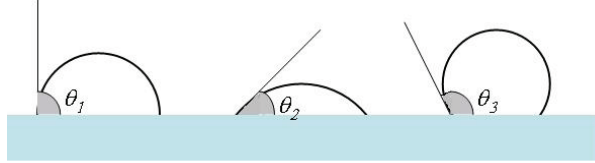
Figure 1.1: Contact angles and wetting. Without any wetting effects, any stable droplet adhering to the wall will be semi-circular and have a contact angle of $\theta = \frac{\pi}{2}$ (left). If the fluid in the droplet is wetting, the contact angle $\theta < \frac{\pi}{2}$ (centre). If the fluid in the droplet is non-wetting, the contact angle $\theta > \frac{\pi}{2}$ (right).

## 1.4   Wetting

In addition to the interfacial forces which exist in two-phase flows, the presence of walls adds another element which affects the flow. Just as surface tension exists between the "red" and "blue" fluid components, there is a tension between each of the fluid components and the wall, and these are likely to be unequal. The phase which experiences a stronger adherence to the wall is described as the *wetting phase*, while the other is the *non-wetting* phase.

When a droplet adheres to a wall, the angle $\theta$ between the tangent line of the droplet at the contact point and the wall is defined as the *contact angle* (figure 1.1). If the fluid of a droplet is wetting, its stronger adherence to the wall means that the droplet will spread out over the wall, increasing its contact area, and decreasing the contact angle. In contrast, a droplet of non-wetting fluid will contract to give a smaller contact area, resulting in a larger contact angle. The fluid in the droplet is called the wetting phase if the contact angle is less than $\frac{\pi}{2}$ and the non-wetting phase if the angle is greater than $\frac{\pi}{2}$. Note that wetting is a relative term, for example a fluid that is wetting with respect to water may be non-wetting with respect to ethanol. Wetting properties are also dependent on the chemical composition of the rock, though in most cases it is assumed that rocks are water-wetting with respect to oil [4].

Mathematically, the contact angle is a function of the components' surface tension coefficients in relation to the wall, $\sigma_{RW}$ and $\sigma_{BW}$, and the mutual surface tension coefficient between the components, $\sigma_{RB}$. Young's equation for the contact angle of a "red" droplet is given by [4]

$$\cos\theta = \frac{\sigma_{BW} - \sigma_{RW}}{\sigma_{RB}}. \tag{1.14}$$

Young's equation requires $|\cos\theta| < 1$, if this is not the case, the wall is totally wetting with respect to one of the phases. If the right hand side of (1.14) is less

than -1, the wall is completely blue wetting and a red droplet will not contact the wall if there is any blue fluid present. If the fraction is greater than 1, a red droplet in contact with the wall will spread out indefinitely [4]. Note that equation (1.14) does not tell the values of the various $\sigma$, merely a relationship between them.

Wetting effects are crucial for a number of fluid phenomena, such as spontaneous imbibition of a wetting fluid into a narrow capillary, and the entrapment of oil in narrow capillaries when a wetting fluid such as water is used to drive the flow [5].

## 1.5 Adsorption

Adsorption is the process in which surfactants are accumulated at interfaces. The substances that tend to accumulate have a molecular structure where opposite ends of the molecule prefer a particular phase. In the special case that water is one of the phases, these ends are called the *hydrophilic* and *hydrophobic* ends. Because of this structure, such molecules will tend to settle at the interface where both components are available.

Adsorption reduces the surface tension, in many cases quite significantly. For a water-air interface, adsorption may reduce the surface tension from 72 mN/m to 30 mN/m. while the surface tension of an oil-water interface may be reduced from 50 mN/m to 5–10 mN/m [6, 7].

Generally, adding more surfactant will continue to reduce the surface tension. However, there is a limit called the *critical micelle concentration* (CMC) when micelles, small clusters of surfactant molecules, will spontaneously form. In water, this means the hydrophilic heads form the surface of the micelle while the tails make up the micelle's interior. These micellar surfactant molecules do not adsorb to the interface and so do not reduce the surface tension further [6].

To understand the relationship between surface tension and surfactant concentration at sub-CMC concentrations, we need to study the theory regarding the free energy of the interface. The Gibbs-Duhem equation for the free energy $dG$ is given by

$$dG = -SdT + Ad\sigma + \sum n_i d\eta_i, \tag{1.15}$$

where $T$ is the temperature, $S$ is the entropy, $n_i$ is the number of moles, $\eta_i$ is the chemical potential, and $\sigma$ is the surface tension coefficient. The entropy term $SdT$ is deducted from the total energy to find the free energy, $Ad\sigma$ is the interfacial energy term, while the last term is energy due to the chemical potential at the interface [3].

If the interface is at equilibrium, the free energy is zero. Further, the entropy

term may be ignored if the temperature is constant. This reduces the Gibbs-Duhem equation to

$$d\sigma = -\sum \frac{n_i}{A} d\eta_i = -\sum \Gamma_i d\eta_i. \tag{1.16}$$

If it is assumed that $\Gamma_i = \frac{n_i}{A} = 0$ for solvent components and non-zero for surfactant components only, equation (1.16) becomes

$$d\sigma = -\Gamma_2 d\eta_2. \tag{1.17}$$

For an ideal solution, the chemical potential $\eta_2$ is given by

$$\eta_2 = \eta_2^0 + RT \ln(Ca_{surf}), \tag{1.18}$$

where $R$ is the ideal gas constant, $a_{surf}$ is the surfactant's activity coefficient and $C$ is the surfactant concentration. Hence,

$$d\eta_2 = RT d(\ln(Ca_{surf})), \tag{1.19}$$

which inserted into equation (1.17) gives the Gibbs adsorption equation [3]

$$\frac{d\sigma}{d(\ln Ca_{surf})} = -\Gamma_2 RT, \tag{1.20}$$

which shows the relationship between the surface tension and the surfactant concentration. If we assume that $\Gamma_2$ is proportional to the concentration, say $\Gamma_z = \kappa C$, the solution of equation (1.20) becomes

$$\sigma = \sigma_0 - \kappa RTC, \tag{1.21}$$

which shows a reduction of the surface tension parameter proportional to the surfactant concentration.

Physical experiments, such as those conducted by Shinoda *et al.* [8], show that the surface tension decreases roughly linearly with the *logarithm* of concentration, then abruptly flattens out when the CMC threshold is crossed.

## 1.6   Surface tension induced movement

A spatial variation in surface tension can induce movement in a two-phase system. This motion was studied by Levich and Krylov [9]. An example studied by Levich and Kuznetzov provides an analytic solution [10]. As previously, there are two phases, "red" and "blue", which have viscosities $\mu^R$ and $\mu^B$. A single circular droplet of red fluid has radius $r$ and a diffusion layer of thickness $\delta_d$. The surrounding fluid is blue. There are no external forces.

If the two phases are not in equilibrium, the equations for the directions normal ($n$) and tangential ($t$) to the interface are given by the equations

$$p^R - p^B + \sigma \left( \frac{1}{r} \right) = 2\mu^R \frac{\partial u_n^R}{\partial n} - 2\mu^B \frac{\partial u_n^B}{\partial n}, \tag{1.22}$$

$$\mu^R \left( \frac{\partial u_n^R}{\partial t} + \frac{\partial u_t^R}{\partial n} \right) - \mu^B \left( \frac{\partial u_n^B}{\partial t} + \frac{\partial u_t^B}{\partial n} \right) = \frac{\partial \sigma}{\partial t}, \tag{1.23}$$

where $u_n^s$ and $u_t^s$ represent the velocity of phase $s$ in the normal and tangential directions respectively [9].

Variation in surface tension mean that the right hand side of equation (1.23) is nonzero, which can only be balanced by having non-zero velocities. This kind of surface tension induced motion is called the Marangoni effect.

Assume now that the concentration $C$ of a stationary surfactant in the domain increases linearly with $x$, with gradient $\frac{dC}{dx}$. The surfactant causes the surface tension to decrease, hence $\frac{\partial \sigma}{\partial C}$ is negative. For a surfactant with the same properties as equation (1.21), $\frac{\partial \sigma}{\partial C} = \kappa$, but the theory does not assume that this relationship is linear.

Since the surface tension at opposite ends of the droplet is imbalanced, the surfactant concentration gradient will cause the droplet to move in the direction of the concentration gradient, with the velocity

$$u = -\frac{(r + \delta_d) \frac{\partial \sigma}{\partial C} \frac{dC}{dz}}{2\mu^B + 3\mu^R - \frac{2C_0 \delta_d}{Dr} \cdot \frac{\partial \sigma}{\partial C}}, \tag{1.24}$$

where $D$ is a diffusion parameter and $C_0$ is the equilibrium surface concentration of the surfactant.


## 1.7   Applications of surfactants

In this section, we will discuss some situations where spatial variation in surface tension is of interest. The focus in the thesis has been the effect such variation has on the flow in porous media. The impact this has on oil recovery makes this an area of high economic importance.

The lattice Boltzmann equation and multiphase flow models is covered in chapters 2 and 3, but areas where LBM has been applied are indicated in this chapter.

### 1.7.1   Use in oil recovery

Oil recovery from deep reservoirs is usually executed by water injection at one end in order to maintain reservoir pressure. The oil in the reservoir is pushed towards the production wells where it can be recovered. At some point, the injected water will also arrive at the production well. If the process was 100% effective, this water-break would signal the complete depletion of the reservoir, but this is not the case. Even after the water break, the reservoir contains a mixture of water and oil. Much of the residual oil may still be recoverable. In fact, almost 2 trillion barrels of conventional, and 5 trillion barrels of heavy oil, may remain in the reservoir after the conventional oil recovery mechanism is complete on a worldwide basis [11].

Oil may be left behind for a variety of reasons, and numerous methods for enhanced oil recovery have been implemented. Some pockets of oil may be trapped in dead ends, or oil droplets may be trapped in a pore space and unable to get into a capillary. One of the first applications of multiphase lattice Boltzmann methods was to simulate the flow of oil and water mixtures in reservoirs, and determine the conditions for which there would be no oil flow [12].

In reservoir theory, two numbers play an important role in determining how much of the oil can be recovered. These are the capillary number

$$N_C = \frac{v\mu}{\sigma}, \tag{1.25}$$

where $v$ is the Darcy velocity, and the water/oil mobility ratio

$$M = \frac{\lambda_w}{\lambda_o}, \tag{1.26}$$

where $\lambda_w$ and $\lambda_o$ are the mobilities (permeability/viscosity ratios) of water and oil respectively. For better oil recovery, the capillary number should be large while the mobility ratio should be small. The capillarity number can be improved by using surfactants that lower the surface tension $\sigma$ while water-soluble polymers can be used to obtain a more favorable mobility ratio [11].

The interest in this thesis has been with oil trapped in pore spaces by surface tension and wetting effects. Pushing a large droplet into a narrow capillary requires a deformation, which creates a pressure gradient which will immobilize the droplet. Reducing these forces is one manner in which more oil can flow through the reservoir and be recovered. Surfactants, and microbial activity are some of the means used to enhance oil recovery.

Considerable theoretical, experimental, and numerical work has been conducted to study the effects of surfactants, depending on the mechanism.

The use of gels in oil fields in order to achieve a disproportionate permeability reduction was studied by Langaas using a free energy scheme (section 3.3.1)[13].

Wetting effects and some simulations with gels were conducted by Langaas and Grubert[14] and further simulations were conducted by Langaas and Nilsson[15].

In some cases, the injection of surfactants can create microemulsions. The flow of oil/water emulsions in narrow capillaries was studied experimentally by Cobos et al. [16]

The effect of microbial activity is similar to that of surfactants, where a biofilm causes changes in interfacial and wetting properties. Lattice Boltzmann simulations of microbial activity were conducted by Hiorth *et al.* [17]

### 1.7.2   Biological applications

In 1976 and 1977 [18, 19], Greenspan conducted laboratory experiments and produced some mathematical models to determine the effect variational surface tension could have on cell cleavage.

Sapir and Nir [20] found that variations in surface tension did produce an elongation of a droplet, but no significant furrowing (cleavage), this result was also found by Li and Lubkin [21] using another numerical model. Typically, a circular droplet will be deformed in the order of 10% when the surface tension is reduced in two ends of the droplet.

# Chapter 2

# The lattice Boltzmann method

Simulations of fluid in this work have been conducted using the lattice Boltzmann method (LBM), first introduced as an extension to the lattice gas method [22].

Fluid flow in porous media may be of interest at different scales. The smallest, microscopic scale deals with simulations of the molecular level, the mesoscopic scale deals with flows in a single pore, the macroscopic scale deals with flow over multiple pores, while the megascopic scale deals with field-scale flow [23]. The lattice Boltzmann method is most suitable for simulations on the mesoscopic or macroscopic scale. Even though the the lattice Boltzmann model is based on molecular gas theory, the *macroscopic* quantities of density and velocity are tracked. The method relies knowledge of the pore structure, but field scale terms such as porosity and permeability are not used directly. However, the permeability of small blocks of porous material may be calculated through lattice Boltzmann simulations [24].

This chapter covers the theory of the lattice Boltzmann method, including the underlying theory and historical development, its connection with the Navier-Stokes equation, and implementation.

## 2.1   Lattice gas predecessor

While the lattice Boltzmann equation is now generally viewed as a discretization of the Boltzmann equation on a regular grid, the model was at first derived from the lattice gas schemes [23].

The lattice gas scheme is a cellular automaton that uses a regular grid and discrete step. If multiple particles are present at a grid cell, they must have different velocities (a requirement called the *exclusion principle*). The number of possible velocities is greatly restricted, commonly the only velocities allowed are those that make a particle move to a neighboring grid cell at the next discrete time step.

At each time step, particles move to another site in accordance with their velocity. If two or more particles arrive at the same site at any given time step, they may collide so that their course is altered.

The collision rules must conserve the total number of particles and momentum. In addition, all collisions are invertible. If particles with velocities $c_1$ and $c_2$ collide, resulting in post collision velocities $c'_1$ and $c'_2$, then there exists an equally probable collision resulting in post-collision velocities $c_1$ and $c_2$. In the simplest cases, pre-collision velocities $c'_1$ and $c'_2$ give the desired inverse collision. Sometimes there is more than one possible collision conserving mass and momentum. When this is the case, one of the collisions is chosen at random. Such models are non-deterministic, but in practice an arbitrary, non-random method is used to determine which collision occurs in ambiguous situations [25].

The lattice gas equation can be written as

$$n_i(\boldsymbol{x} + \boldsymbol{c}, t + 1) - n_i(\boldsymbol{x}, t) = \Omega_i(n), \tag{2.1}$$

where the left hand side describes streaming and the right hand side is the collision rule. The Boolean variable $n_i$ is 1 if there is a particle on direction $i$, and 0 otherwise.

The first such scheme was proposed by Hardy, Pomeau, and de Pazzis, [26, 27, 28], hence the name "HPP" model. This scheme involves a square lattice, where each cell had the capacity for four particles. The possible particle velocities are $(1,0), (0,1), (-1,0)$ and $(0,-1)$. If particles collide head on, they turn and move out at right angles to their incident velocity. The HPP model is easy to implement, and Hardy et al. were able to recover some fluid properties in the model, but the model lacks isotropy and rotational invariance. The square lattice does not account for enough directions simultaneously to substitute for a circle [23].

Although the square lattice is insufficient for isotropic flow, more satisfactory simulations by lattice gas methods are possible by using a hexagonal lattice (triangular if the particles occupy the nodes rather than cells), so that each site connects to six neighbors. The method with the hexagonal lattice is called the Frisch, Hasslacher, and Pomeau (FHP) model after its proposers in 1986 [29] (note that Frisch *et al.* called the model "hexagonal lattice gas" or "HLG"). Other versions on a hexagonal grid include rest particles, which means each site can host up to seven particles.

Even with the improved hexagonal lattices, some drawbacks with the lattice gas approach remain. The state at each site and velocity is Boolean instead of continuous. Whether or not a particle is at a particular site is random, and the results are therefore burdened with noise. Averaging over several sites alleviates, but does not eliminate, the problem.

Lattice gas models generally lack Galilean invariance (independence of inertial frame of reference). The most serious consequence is that a vortices in the fluid
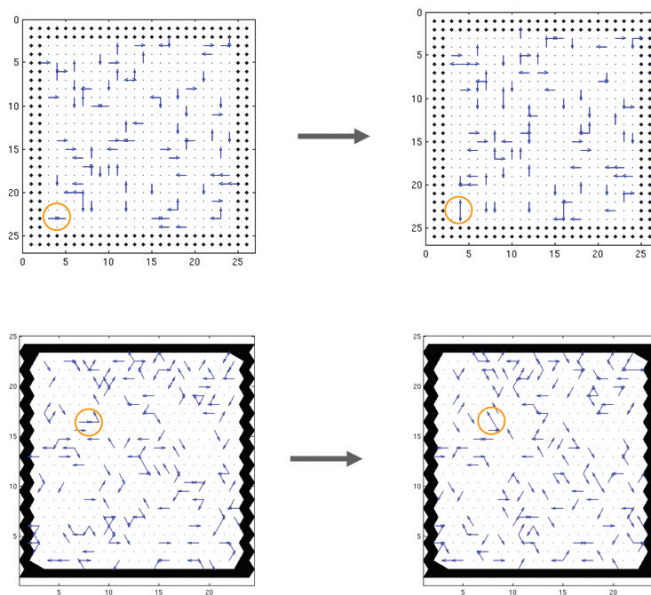
Figure 2.1: Snapshots of the location and velocity of particles at two consecutive time steps in a sample lattice gas simulations. The top two figures show an example of the evolution in an HPP model, the bottom two figures show the evolution in an FPP-I model. The circles indicate one of the collisions taking place between these particular time steps.

advect with a different velocity than the other fluid. Some models have been developed to attend to that issue [30].

Extending the method to three dimensions is difficult, because of the lack of a suitably isotropic lattice. This problem can be worked around, as shown by d'Humieres *et al.* [31] by adding a fourth dimension and utilising a hypercubic lattice. One of the dimensions is a "ghost" dimension. This technique makes the method computationally very complex. In the hypercube model, each node connects to 24 neighbors, so there are a possible $2^{24}$ states possible at each site and so handling the collision operator by means of a look-up table is no longer feasible [23].

The FHP was extensively analyzed by Wolfram [32], and it was shown that the Navier-Stokes equations could be derived from the method. In the derivation, an

average of $n_i$, denoted $f_i$ is defined:

$$f_i = \langle n_i \rangle \tag{2.2}$$

where $\langle \cdot \rangle$ denotes a space-time average. $f_i$ is called the distribution function, and is covered in Section 2.2. Averaging equation (2.1) to involve $f_i$ is actually the earliest derivation of the lattice Boltzmann equation, although it was not initially viewed as a method in its own right.

The Navier-Stokes equations can be derived through the Chapman-Enskog expansion, similar to what will be shown in Section 2.7. The specifics which pertain to the lattice gas method are covered by Wolf-Gladrow [25] Section 3.2.6.

The first lattice Boltzmann model was developed in 1988 by McNamara and Zanetti [22]. The idea was to replace the Boolean values of lattice gas models with floating point numbers, representing average distributions as in (2.2). This avoids the noise problem. As in the lattice gas models, the collision rules conserve density and momentum, however the collisions are not invertible.

He and Luo later showed that the lattice gas foundations were not needed, and that the lattice Boltzmann method could be derived directly from discretizing the Boltzmann equation [33, 34].

## 2.2   The distribution function

Particle movement in a gas or fluid with $N$ particles with mass $m$ is subject to Newton's laws of motion. In principle the movement of each molecule as it is subjected to collisions and other forces can be tracked. However, one mole of gas contains $6.02 \times 10^{23}$ molecules, and the sheer number of particles makes it impossible to record each molecule individually except for extremally thin gas.

Fortunately, the tracking process can be simplified. In a gas, particles move at many different velocities, but not all velocities are equally probable. We can introduce a probability distribution $p(\boldsymbol{x}, \boldsymbol{c}, t)$ telling the probability of a particle at site $\boldsymbol{x}$ at time $t$ moving at velocity $\boldsymbol{c}$. If there are $n$ particles, the *distribution function* $f(\boldsymbol{x}, \boldsymbol{c}, t) = np(\boldsymbol{x}, \boldsymbol{c}, t)$ is used to track how many particles at a site $\boldsymbol{x}$ at time $t$ are moving with a velocity $\boldsymbol{c}$.

Macroscopic quantities can be found from integrating moments of the distribution function. The density of a gas $\rho$ can be found by

$$\rho(\boldsymbol{x}, t) = \int m f(\boldsymbol{x}, \boldsymbol{c}, t) d\boldsymbol{c}. \tag{2.3}$$

The movement of particles means there is kinetic energy in the gas. If the sum of all the particle velocities is nonzero, the entire gas as a body moves at the

macroscopic velocity $\boldsymbol{u}$, distinguished from the individual particle velocity $\boldsymbol{c}$. In most cases $||\boldsymbol{u}|| \ll ||\boldsymbol{c}||$. The momentum is given by

$$\rho(\boldsymbol{x},t)\boldsymbol{u}(\boldsymbol{x},t) = \int m\boldsymbol{c}f(\boldsymbol{x},\boldsymbol{c},t)d\boldsymbol{c}. \tag{2.4}$$

The remaining particle movement, $\boldsymbol{c} - \boldsymbol{u}$ is disordered, and makes up the thermal energy given by

$$\frac{3}{2}nkT = \int \frac{1}{2}m(\boldsymbol{c}-\boldsymbol{u})^2 \cdot f(\boldsymbol{x},\boldsymbol{c},t)d\boldsymbol{c}, \tag{2.5}$$

where $T$ is the temperature and $k$ is Boltzmann's constant, $k = 1.3807 \times 10^{-23} J/K$.

## 2.3 The Boltzmann equation

The Boltzmann equation was derived by Ludwig Boltzmann in 1872, and is one of the most important results in theoretical physics [23]. In its most basic form, the equation is given as

$$\frac{\partial f}{\partial t} + \boldsymbol{c} \cdot \frac{\partial f}{\partial \boldsymbol{x}} + \boldsymbol{a} \cdot \frac{\partial f}{\partial \boldsymbol{c}} = \Omega(f), \tag{2.6}$$

where the left hand side represents the total derivative of the distribution function subjected to the external force that gives acceleration $\boldsymbol{a}$. This accounts for the streaming of particles. The right hand side $\Omega(f)$ is a collision operator and accounts for collisions between particles.

The streaming part of the equation can be derived by considering what happens if an external force $\boldsymbol{F}$ acts on each of the particles in the fluid. We follow the derivation presented by Buick [35]. By Newton's second law, we have the acceleration $\boldsymbol{a} = \frac{\boldsymbol{F}}{m}$. After a short time interval $dt$, the new distribution function will be $f(\boldsymbol{x}+\boldsymbol{c}dt, \boldsymbol{c}+\boldsymbol{a}dt, t+dt)$. In the absence of collisions, these are the same particles as before the time step $dt$, so $f(\boldsymbol{x}+\boldsymbol{c}dt, \boldsymbol{c}+\boldsymbol{a}dt, t+dt)d\boldsymbol{x}d\boldsymbol{c}$ and $f(\boldsymbol{x},\boldsymbol{c},t)d\boldsymbol{x}d\boldsymbol{c}$ should be equal. The fact that they are not equal in reality, is due to interparticle collisions, which we write as $\Omega(f)d\boldsymbol{x}d\boldsymbol{c}dt$, and we obtain

$$f(\boldsymbol{x}+\boldsymbol{c}dt, \boldsymbol{c}+\boldsymbol{a}dt, t+dt)d\boldsymbol{x}d\boldsymbol{c} - f(\boldsymbol{x},\boldsymbol{c},t)d\boldsymbol{x}d\boldsymbol{c} = \Omega(f)d\boldsymbol{x}d\boldsymbol{c}dt. \tag{2.7}$$

Dividing (2.7) by $d\boldsymbol{x}d\boldsymbol{c}dt$ and letting $dt \to 0$ will finally yield the classical Boltzmann equation (2.6).

The collision operator depends on the two-body distribution function $f_{12}$, which represents the probability of finding a particle of velocity $\boldsymbol{c}_1$ around site $\boldsymbol{x}_1$, while simultaneously finding a particle of velocity $\boldsymbol{c}_2$ around site $\boldsymbol{x}_2$.

In order to avoid having to deal with three-particle collisions, Boltzmann assumed that the particles were point-like, structureless, and that collisions were interactions over much shorter ranges than the mean distance between particles. A consequence of this is the assumption that particles prior to collision are uncorrelated, and that the events governed by the distribution functions $f_1$ and $f_2$ are independent. This gives Boltzmann's closure assumption: [23]

$$f_{12} = f_1 f_2. \tag{2.8}$$

The Boltzmann equation with a full collision operator is therefore [23]

$$\frac{\partial f}{\partial t} + \boldsymbol{c} \cdot \frac{\partial f}{\partial \boldsymbol{x}} + \boldsymbol{a} \cdot \frac{\partial f}{\partial \boldsymbol{c}} = \int (f_1' f_2' - f_1 f_2) |g| b(\boldsymbol{g}, \theta) \, db \, d\theta \, d\boldsymbol{c}_2, \tag{2.9}$$

where $\boldsymbol{g}$ is the relative velocity between the particles, and $\theta$ is the collision angle. The impact parameter of an individual particle is denoted $b$. Primes indicate post-collision distributions.

## 2.3.1 Equilibrium distribution and the BGK collision operator

Collisions are reversible, so if two particles with velocities $\boldsymbol{c}_1$ and $\boldsymbol{c}_2$ collide so that the post collision velocities are $\boldsymbol{c}_1'$ and $\boldsymbol{c}_2'$, then two particles colliding with velocities $\boldsymbol{c}_1'$ and $\boldsymbol{c}_2'$ will result in post-collision velocities of $\boldsymbol{c}_1$ and $\boldsymbol{c}_2$. Since underlying processes are reversible, the macroscopic processes in the gas could in principle seem to be reversible as well. However, the vast number of correct collisions needed to reverse a macroscopic gas process make such an event extremely unlikely. In fact, Boltzmann's $H$-theorem which deals with the quantity

$$H = \int f \ln f \, d\boldsymbol{c}, \tag{2.10}$$

shows that $H$ will never increase. On the other hand, $H$ is bounded below, so at some point $H$ will be at its minimum [36]. Hence, a central concept is that of an equilibrium distribution $f^M$, where the collision operator does not have any effect.

$$\Omega(f^M, f^M) = 0. \tag{2.11}$$

This means that $f_{12} = f_{12}'$, or using the closure assumption (2.8) and taking logarithms on both sides gives

$$\ln f_1'^M + \ln f_2'^M = \ln f_1^M + \ln f_2^M. \tag{2.12}$$

This collision invariance for $\ln f$ shows that it is a function of the other collision invariant quantities (particle number, momentum, and kinetic energy), and can be

written as a polynomial [23]

$$\ln f^M = A + B_a c_a + \frac{1}{2} C c^2, \tag{2.13}$$

where the parameters $A$, $B$ and $C$ can be determined by using the distribution function definitions of density, momentum and kinetic energy together with Gaussian quadrature. The resulting expression for $f^M$ is

$$f^M = n \left( \frac{m}{2\pi kT} \right)^{D/2} e^{-mc^2/2kT}, \tag{2.14}$$

where $D$ is the number of dimensions. The distribution $f^M$ is called the Maxwell distribution. Note that the Maxwellian represents a gas which is macroscopically at rest.

For a gas with a macroscopic velocity $\boldsymbol{u}$, a local equilibrium distribution $f^{eq}$ can be defined:

$$f^{eq} = n \left( \frac{m}{2\pi kT} \right)^{D/2} e^{-m((\boldsymbol{c}-\boldsymbol{u})^2/2kT)}. \tag{2.15}$$

The existence of the local equilibrium distribution has been exploited to make the simplified collision operator $\Omega_{BGK}$ where "BGK" are the initials of its proposers Bhatnagar, Gross, and Krook who introduced it in 1954. The operator is given by [37]

$$\Omega_{BGK} = -\frac{1}{\tau}(f - f^{eq}), \tag{2.16}$$

where $\tau$ is a relaxation time parameter. The BGK operator works on the assumption that the distribution is dominated by equilibrium terms, and that the non-equilibrium is a small correction.

## 2.4   Basic theory of the lattice Boltzmann equation

The remainder of this chapter will deal with the theory of the lattice Boltzmann method for a single phase and component. Extensions to more complex fluids are covered in Chapter 3.

The lattice Boltzmann method was originally proposed by McNamara and Zanetti [22] based on the lattice gas method described in Section 2.1, although modern interpretations view the method as a discretization of the Boltzmann equation in Section 2.3. As in the lattice gas method, the lattice Boltzmann runs on a discrete lattice, and evolves in a streaming and collision framework with time step $\delta_t$.

Among the major drawbacks of the lattice gas method were statistical noise and lack of Galilean invariance. Statistical noise comes due to the position of particles

being discrete and in a sense "random", while the exclusion principle causes the breakdown of Galilean invariance. The lattice Boltzmann method resolves both these problems. The Boolean variable $n_i$ is replaced by the distribution function $f_i$. Although $f_i$ is discreticized in space and time, $f_i$ itself is a continuous function, so statistical noise is eliminated. Although space, time, and velocity remain discreticized, the exclusion principle from the lattice gas method is abolished, and there are no limitations on how many particles may possess a given velocity at any given site and time, so $f_i$ is not limited to be less than 1. The lattice Boltzmann methods therefore do not suffer from Galilean invariance.

### 2.4.1   Lattices

Qian *et. al.* [38] introduced the lattice classification system which has become standard. Each grid is classified on a D$MQN$ scheme, where $M$ is the dimension of the grid, and $N$ is the number of neighbors (including itself if applicable) which particles can move to.

The velocity vectors that connect neighbouring sites to each other are designated $e_i$. The index $i$ represents a direction and $i = 0$ represents the zero-vector.

In a two-dimensional system, the lattices are either square or triangular/hexagonal. Rest particles are almost universally used with the square lattice, and these models are referred to as D2Q9. The triangular lattices are D2Q6 or D2Q7 depending on whether rest particles are present.

Since the hexagonal D2Q6 and D2Q7 lattices have fewer velocities than the square D2Q9 lattice, the hexagonal methods are slightly faster. However, the square lattice is more flexible when it comes to defining boundary conditions, and it is this lattice which has been used in this work.

The three dimensional lattices are always cubical, and usually employ rest particles. A site has 26 possible neighbours, representing the cell's six faces, twelve edges, and eight corners. Generally, all the common three-dimensional lattice Boltzmann models allow the particles to move to one of the six nearest neighbours. The D3Q15 model also lets particles move to one of the eight neighbors sharing a corner, but disallow movement to the neighbors sharing an edge. The D3Q19 model lets particles move to the twelve neighbours sharing an edge, but not to the neighbors sharing a corner. The D3Q27 model allows movement to all the neighbors.

The six two- and three-dimensional lattices mentioned are shown graphically in Figure 2.2.
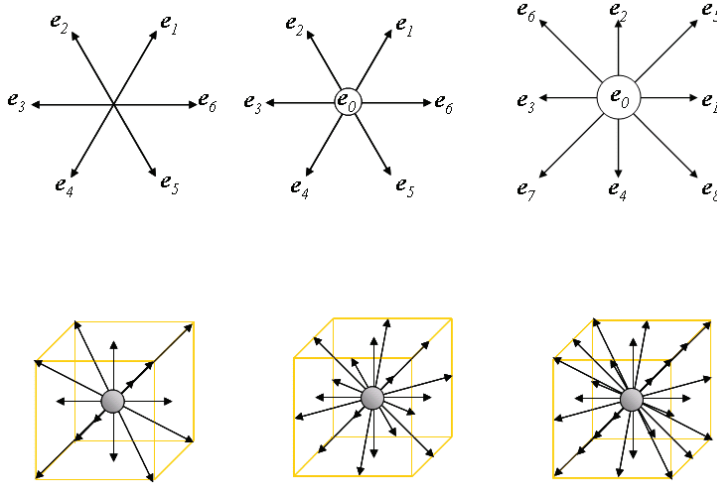
Figure 2.2: Various common lattices for lattice Boltzmann simulations. Top left: D2Q6. Top centre: D2Q7. Top right: D2Q9. Bottom left: D3Q15. Bottom centre: D3Q19. Bottom right: D3Q27.

## 2.4.2   Lattice Boltzmann equation

If we assume a single component fluid and no external forces, the lattice Boltzmann equation can be written as

$$f_i(\boldsymbol{x} + \boldsymbol{e}_i \delta_t, t + \delta_t) - f_i(\boldsymbol{x}, t) = \Omega_i(f). \tag{2.17}$$

This equation has a very similar structure to the lattice gas equation (2.1), but since the variables $f$ are floating point numbers rather than Boolean figures, the collision operator can no longer be executed through a look-up table. The construction of the collision operator comes through applying the theory of the Boltzmann equation with a collision operator similar to the one in equation 2.9. However, the collision step can be considerably simplified by applying the BGK collision operator (2.16). This is referred to as the LBGK (Lattice Bhatnagar-Gross-Krook) method. With this scheme, the collision operator $\Omega_i(f)$ is given by [23]

$$\Omega_i(f) = -\frac{\delta_t}{\tau}(f_i - f_i^{eq}), \tag{2.18}$$

where for low Mach numbers, $f_i^{eq}$ is written as a polynomial of $\boldsymbol{u}$.

For square lattices, the explicit polynomial with particle mass $m = 1$ is given by [34]

$$f^{eq} = w_i \rho \left( 1 + \frac{3(e_i \cdot u)}{c_s^2} + \frac{9(e_i \cdot u)^2}{2c_s^4} - \frac{3u^2}{2c_s^2} \cdot \right) \tag{2.19}$$

where $c_s = \sqrt{3RT}$ [34]. For the triangular six and seven speed lattices, the equilibria are given by

$$f^{eq} = \begin{cases} w_i \rho \left( 1 + \frac{2(e_i \cdot u)}{c^2} + \frac{4(e_i \cdot u)^2}{c^4} - \frac{u^2}{c^2} \cdot \right) & i = 1, \ldots, 6 \\ w_i \rho \left( 1 + \frac{4(e_i \cdot u)}{c^2} + \frac{8(e_i \cdot u)^2}{c^4} - \frac{2u^2}{c^2} \cdot \right) & i = 0, \ldots, 6 \end{cases} \tag{2.20}$$

The weights $w_i$ that come up are related to Gaussian quadrature of velocity integrals, and they depend on the underlying lattice. The weights for the most popular two- and three-dimensional lattices are shown in table 2.1.

| Lattice/Vector length | 0 (rest) | $c$ | $c\sqrt{2}$ | $c\sqrt{3}$ |
|:---:|:---:|:---:|:---:|:---:|
| D2Q6 | – | 1/6 | – | – |
| D2Q7 | 1/2 | 1/12 | – | – |
| D2Q9 | 4/9 | 1/9 | 1/36 | – |
| D3Q15 | 2/9 | 1/9 | – | 1/72 |
| D3Q19 | 1/3 | 1/18 | 1/36 | – |
| D3Q27 | 8/27 | 2/27 | 1/54 | 1/216 |

Table 2.1: Vectors and weights for different lattices. $c$ is the length of the velocity vectors to the nearest neighbors. A dash ('–') means that the lattice does not have any velocity vectors of that length.

The LBGK scheme is the simplest, and most effective lattice Boltzmann scheme. The drawback is that mass, momentum and heat transfer are all governed by the same parameter [23].

The moments for density and momentum are calculated as sums over the discrete distribution function.

$$\rho = \sum_i f_i \tag{2.21}$$

$$\rho u = \sum_i f_i e_i, \tag{2.22}$$

and are shown in Section 2.7 to fulfill the Navier-Stokes equation for weakly non-uniform fluid systems.

The discretization of the Boltzmann equation conducted by He and Luo [33, 34] involves a time discretization, an approximation of the Maxwellian equilibrium

distribution, and a discretization of phase space. The time discretization involves an integral of the continuous Boltzmann equation written in total derivative form

$$\frac{df}{dt} + \frac{1}{\tau'}(f - f^M) = 0,$$ (2.23)

over a time step $\delta_t$, including terms of up to $O(\delta_t)$, giving

$$
\begin{aligned}
f(\boldsymbol{x} + \boldsymbol{c}\delta_t, \boldsymbol{c}, t + \delta_t) &= \frac{1}{\tau'}e^{-\delta_t/\tau'}\int_0^{\delta_t} e^{s/\tau'} f^M(\boldsymbol{x} + \boldsymbol{c}s, \boldsymbol{c}, t + s)ds \\
&\quad + e^{-\delta_t/\tau'} f(\boldsymbol{x}, \boldsymbol{c}, t), \\
&= \frac{1}{\tau'}e^{-\delta_t/\tau'}\int_0^{\delta_t} \left[ e^{s/\tau'}(1 - \frac{s}{\delta_t}) f^M(\boldsymbol{x}, \boldsymbol{c}, t) \right. \quad (2.24) \\
&\quad \left. + \frac{s}{\delta_t} f^M(\boldsymbol{x} + \boldsymbol{c}\delta t, \boldsymbol{c}, t + \delta_t) + O(\delta_t^2) \right] ds \\
&\quad + e^{-\delta t/\tau'} f(\boldsymbol{x}, \boldsymbol{c}, t),
\end{aligned}
$$ (2.25)

where the $O(\delta_t^2)$ terms are ignored. The result is the time discrete Boltzmann equation

$$f(\boldsymbol{x} + \boldsymbol{c}\delta_t, \boldsymbol{c}, t + \delta_t) = f(\boldsymbol{x}, \boldsymbol{c}, t) - \frac{1}{\tau}[f(\boldsymbol{x}, \boldsymbol{c}, t) - f^M(\boldsymbol{x}, \boldsymbol{c}, t)],$$ (2.26)

where $\tau = \frac{\tau'}{\delta_t}$.

The equilibrium distribution function $f^M$ can for low Mach numbers be approximated by $f^{eq}$, given by

$$f^{eq} = \frac{\rho}{(2\pi RT)^{D/2}} \exp(-\boldsymbol{c}^2/2RT) \left[ 1 + \frac{\boldsymbol{c} \cdot \boldsymbol{u}}{RT} + \frac{(\boldsymbol{c} \cdot \boldsymbol{u})^2}{2(RT)^2} - \frac{\boldsymbol{u}^2}{2RT} \right],$$ (2.27)

where terms of $O(\boldsymbol{u}^3)$ and higher are neglected.

The phase space discretization is done so that the moments (2.21) and (2.22) are accurate for $f^{eq}$. This means equating continuous moment integrals of (2.14) with a discrete summation, in particular,

$$\frac{1}{\rho} \int f^M \prod_\alpha c_{i\alpha} d\boldsymbol{c} = \sum_i w_i \prod_\alpha e_{i\alpha},$$ (2.28)

must hold for as high an order of $c_{i\alpha}$ and $e_{i\alpha}$ as possible. This is possible up to the fourth order.

The derivation of $w_i$ for the D2Q9 lattice can be found in Wolf-Gladrow, Section 5.2.1 [25]. The symmetry of the lattice mandates that the weights on vectors with

length $c$ are equal, as are the weights on vectors with length $\sqrt{2}c$, that means $w_1 = w_2 = w_3 = w_4 = w_a$ and $w_5 = w_6 = w_7 = w_8 = w_b$. The odd moments in (2.28) are all zero, while the nonzero even moments give:

$$\sum w_i = w_0 + 4w_a + 4w_b \;=\; 1 \tag{2.29}$$

$$\sum e_{i1}^2 w_i = \sum e_{i2}^2 w_i = 2c^2 w_a + 4c^2 w_b \;=\; \frac{kT}{m} \tag{2.30}$$

$$\sum e_{i1}^4 w_i = \sum e_{i2}^4 w_i = 2c^4 w_a + 4c^4 w_b \;=\; 3\left(\frac{kT}{m}\right)^2 \tag{2.31}$$

$$\sum e_{i1}^2 e_{i2}^2 w_i = 4c^4 w_b \;=\; \left(\frac{kT}{m}\right)^2 \tag{2.32}$$

Comparing equations (2.30)–(2.31) shows that $\frac{kT}{m} = \frac{c^2}{3}$. Plugging this into the last equation shows that $w_b = \frac{1}{36}$. Equation (2.30) (or equation (2.31)) then yields $w_a = \frac{1}{9}$, and finally equation (2.29) gives $w_0 = \frac{4}{9}$.

Multiplying the $w_i$ weights with $\pi$ correspond to the products of the nodes and weights used in Gaussian quadrature when evaluating the integrals in (2.28).

### 2.4.3   Multiple relaxation time methods

The BGK collision operator is the most common way of simulating the relaxation, and the one used throughout this thesis. A more general method is the multiple-relaxation time method (MRT), also called "generalized lattice Boltzmann". The cited advantages of the MRT method are improved numerical stability and increased flexibility which allows variations in the Prandtl number (viscous diffusivity rate/thermal diffusivity rate), and the kinematic to bulk viscosity ratio [39]. The cost is increased computationally complexity and longer calculation times.

As with the BGK operator, the MRT operator features a relaxation to equilibrium, but instead of the scalar multiplier $\frac{1}{\tau}$ used in equation (2.18), the MRT multiplies $f - f^{eq}$ with a $N \times N$ matrix $S$ (we recall from Section 2.4.1 that $N$ is the number of discrete velocities in the lattice). Each of the $N$ rows in $S$ represents a different moment. For example, the nine moments accounted for in an MRT simulation on a D2Q9 lattice can be density, energy, energy squared, $x-$ and $y-$momentum, $x-$ and $y-$heat fluxes, and the stresses $p_{xx}$ and $p_{xy}$ [40]. The special case where $S$ is given by $\frac{1}{\tau}I$, where $I$ is the $N \times N$ identity matrix, corresponds to the BGK method [39].

## 2.5   Boundary conditions

Boundary conditions set conditions for movement in the region in which the fluid flows, and are therefore highly important in all fluid simulations.

Walls are by definition impenetrable, and unless we want to place a source or sink, fluid particles should not enter or come out of wall nodes. Hence, the macroscopic velocity component normal to the wall should be zero. In addition, viscous fluids at low velocity will usually have no flow parallel to the wall as well (no slip).

Another type of boundary condition is required at the fluid edge of domains where particles can enter and exit the domain. We discuss two ways of handling these, periodic boundary conditions and open boundaries with a fixed pressure or velocity.

Even for fairly complex boundaries, the implementation of boundary conditions is quite simple in lattice Boltzmann methods. This asset gives the lattice Boltzmann method an edge in, for example, porous media simulations where boundaries can be very complicated.

### 2.5.1   Bounce-back boundary condition

The bounce-back condition is the standard no-slip condition used for boundaries between fluids and walls. The premise for the bounce-back condition is that all particles hitting a wall node reverse their direction to move back on the vector in which they entered.

In practice, this is implemented as part of the propagation process. Fluid particles may not enter a wall node, if the particles are on course to enter a wall node their course is reversed. For example, assume a particle at $(x, y)$ moving on the $e_5$-vector (northeast). The propagation for this particle is given in pseudo-code as

```
if wall(x+1,y+1) == 1
  fpre(x,y,7) = fpost(x,y,5);
else
  fpre(x+1,y+1,5) = fpost(x,y,5);
end
```

Here, "fpre" and "fpost" indicate pre-relaxation and post-relaxation distributions respectively. The if condition is met if the node in the northeast is a wall node, and the particle is therefore reflected to vector $e_7$ (southwest). Otherwise, the else-statement is normal propagation of the particle.

To envision that the bounce-back condition yields a no-slip boundary, one can imagine that there is a an imaginary particle in the wall emerging from the wall,

moving opposite to the particle entering, the resulting distribution in the fluid is the same. The sum of momentum for the incoming and the imaginary outgoing particle is zero [41].

The accuracy of the bounce-back condition is dependent on how well the wall fits the real geometry. If there is an exact match between the physical and boundaries, with the wall passing through the middle of the fluid and wall node, the bounce-back condition is second-order accurate, the same as the LBGK equation itself. This includes simple flows such as Poiseuille flow (pressure driven flow between two parallel plates) [42]. However, if the physical boundary is not aligned with the lattice, and needs to be approximated by staircasing, the boundary itself is only first-order accurate. This is indeed the greatest drawback to the bounceback scheme in simulations, and various interpolation schemes to improve the accuracy to second order have been proposed, for example Noble *et al.* [43]. With second order accuracy, a lower grid resolution may be permitted. The actual accuracy of such methods were investigated by Maier and Bernard [44], who found that these interpolation schemes were second order accurate for well-defined flows with small gradients. Maier and Bernard also considered the conditions in which the improved accuracy justifies the increased complexity of the boundary implementation.

Note that implementing the boundary conditions is a very simple task in the lattice Boltzmann method. The algorithm used to enforce the boundary requires only the obstacle positions, and is just as fast for tortuous and complicated boundaries as it is for simple boundaries. Because of the ease in which complicated boundaries can be implemented, the lattice Boltzmann method is an important method for fluid flow through porous media [45].

### 2.5.2  Periodic boundary conditions

In some cases, problems with the edge of the domain can be handled by implementing periodic boundary conditions. In effect, such conditions remove edges altogether by ensuring that all nodes have neighbouring nodes on all sides. A node on the top "edge" is connected to the nodes on the bottom edge.

These conditions are especially effective for cases where surface effects are not significant [23].

In some cases, periodic conditions are insufficient however. With periodic boundary conditions, any particle leaving the domain, will immediately reenter at the opposite side. This means that in a classic two-phase scenario with a water mass pushing an oil mass through a channel, oil exiting at the outlet will appear at the inlet which is not desirable. In addition, it is not possible to implement a pressure boundary condition at the inlet and outlet without creating a discontinuity.

### 2.5.3 Open boundary conditions

If we want to allow particles to enter and exit the domain, we need a way to handle open boundaries. Nodes at the edge are called *inlets* and *outlets*, depending on whether there is a net flux in or out of the domain at these nodes. Note however, that except for the extreme high-Mach flows, there are always many particles moving against the flow, so there will be particles leaving a domain at the inlet and particles entering the domain at the outlet.

We have generally used the method described by Zou and He [46] to simulate open boundaries. The method here can handle both velocity boundary conditions, with fixed velocities $\boldsymbol{u}_{in}$ and $\boldsymbol{u}_{out}$ at these nodes, and pressure boundary conditions, with fixed pressures $p_{in}$ and $p_{out}$ at the inlet and outlet nodes. Pressure is given as a function of density, so pressure boundary conditions are equivalent to density boundary conditions.

The problem in open boundaries lies in identifying the distribution components that point from the inlet and outlet into the domain. Regular propagation determines the figures for the remaining distribution components, including the particles leaving the domain. For example, for a D2Q9 lattice, on a boundary at the left of the domain, the unknown distribution components are $f_1$, $f_5$, and $f_8$.

If we first address the velocity boundary condition, we have four unknowns, the three distribution components $f_{1,5,8}$ which we want to determine, and the density $\rho$. From the definitions of density and velocity, three equations are immediately apparent,

$$f_1 + f_5 + f_8 = \rho - f_0 - f_2 - f_3 - f_4 - f_6 - f_7, \tag{2.33}$$
$$f_1 + f_5 + f_8 = \rho u_x + f_3 + f_6 + f_7, \tag{2.34}$$
$$f_5 - f_8 = \rho u_y - f_2 + f_4 - f_6 + f_7. \tag{2.35}$$

In order to obtain a fourth equation and close the system, Zou and He assumed that the nonequilibrium part of the distribution was reflected at the boundary.

$$f_1 = f_3 + f_1^{eq} - f_3^{eq}. \tag{2.36}$$

With equations (2.33-2.36), the unknowns are given by:

$$\rho = \frac{1}{1 - u_x}(f_0 + f_2 + 2f_3 + f_4 + 2f_6 + 2f_7), \tag{2.37}$$

$$f_1 = f_3 + \frac{2}{3}\rho u_x, \tag{2.38}$$

$$f_5 = f_7 + \frac{1}{2}(f_4 - f_2) + \frac{1}{6}\rho u_x + \frac{1}{2}\rho u_y, \tag{2.39}$$

$$f_8 = f_6 + \frac{1}{2}(f_2 - f_4) + \frac{1}{6}\rho u_x - \frac{1}{2}\rho u_y. \tag{2.40}$$

Similar results can be found for inlets and outlets at the top, bottom, and right side of the domain.

If we move on to pressure, or density boundary conditions, the first realisation is that fixing the pressure only is insufficient. It is also necessary to fix the velocity parallel to the inlet or outlet to obtain enough equations, which is a drawback with the Zou and He method. Usually, we assume that the flow is normal to the inlet and outlet, for the left boundary that means $u_y = 0$.

As with the velocity boundary conditions, we use the equations for density and velocity, and assume bounce-back of the nonequilibrium part to close the system. The resulting equations for the left boundary are

$$f_1 + f_5 + f_8 = \frac{1}{1-u_x}(f_0 + f_2 + 2f_3 + f_4 + 2f_6 + 2f_7), \qquad (2.41)$$

$$f_5 - f_8 = u_y - f_2 + f_4 - f_6 + f_7, \qquad (2.42)$$

$$f_1 + f_5 + f_8 = \rho u_x - f_3 - f_6 - f_7, \qquad (2.43)$$

$$f_1 = f_3 + f_1^{eq} - f_3^{eq}, \qquad (2.44)$$

and the result is

$$u_x = 1 - \frac{1}{\rho}(f_0 + 2f_1 + f_2 + f_4 + 2f_5 + 2f_8), \qquad (2.45)$$

$$f_1 = f_3 + \frac{2}{3}\rho u_x, \qquad (2.46)$$

$$f_5 = f_7 + \frac{1}{2}(f_4 - f_2) + \frac{1}{6}\rho u_x, \qquad (2.47)$$

$$f_8 = f_6 + \frac{1}{2}(f_2 - f_4) + \frac{1}{6}\rho u_x. \qquad (2.48)$$

A general problem with pressure (density) and velocity boundary conditions in general are that they handle two-phase flow badly. At the interface of a two-phase system, the particle density is significantly lower than elsewhere, and this conflicts with the fixed densities $\rho_{in}$ and $\rho_{out}$ if we are using a pressure boundary conditions. In addition, in the lattice flow, we have strong macroscopic currents pointed away from the interface, and these conflict with the fixed velocities $\boldsymbol{u}_{in}$ and $\boldsymbol{u}_{out}$ if we are using velocity boundary conditions.

## 2.6   Implementation

### 2.6.1   Streaming and collision

In the actual simulation, equation (2.17) is evaluated in a two-step process referred to as *streaming* and *relaxation*.

The streaming step handles the propagation of particles, that is, the left hand side of equation (2.17). Boundary conditions, which we covered in Section 2.5 are also handled in the streaming step. This process only involves moving the distribution figures, and require no floating point operations, so this step is usually handled very quickly.

The relaxation step handles the interparticle collisions, that is, the collision term comprising the right hand side of equation (2.17). If the LBGK term in equation (2.18) is used, this process involves calculating the density and momentum by equations (2.21) and (2.22) so that the equilibrium distribution (2.19) can be calculated, before the collision operator is used to calculate the post-collision distributions. These calculations must be made for each site. The large number of floating point operations required makes the relaxation step the most time consuming step in lattice Boltzmann simulations. Fortunately, the collision process in each node happens independently of the process in all the other nodes, so a parallel computer with $n$ processors will speed up the process by a factor $n$ assuming that the full capability of all processors is used simultaneously.

In phase and component flow, there are different components requiring additional distribution functions to represent them. The streaming step is executed for each of those components individually. Interactions between the components are accounted for in the collision step.

External forces such as gravity may be handled in a number of different ways. Four of these are covered in Buick's thesis [35]. In our model, external forces $\boldsymbol{F}$ are calculated by using an altered velocity $\boldsymbol{u}'$ given by

$$\boldsymbol{u}' = \boldsymbol{u} + \frac{\tau}{\rho}\boldsymbol{F} \tag{2.49}$$

when the equilibrium distribution is calculated. External forces are therefore handled as part of the relaxation step. The reason for this selection is that a fairly large force can be simulated, and that it is consistent with force term implementation of the Shan-Chen model for two-phase flow which will be covered in the next chapter.

With an external force, the lattice Boltzmann equation (2.17) with the BGK collision operator (2.18) becomes [25]:

$$f_i(\boldsymbol{x}+\boldsymbol{e}_i\delta_t, t+\delta_t) - f_i(\boldsymbol{x},t) = -\frac{\delta_t}{\tau}(f_i - f_i^{eq}) + \frac{\delta_t c_{\alpha i}}{12c^2}[F_\alpha(\boldsymbol{x},t) + F_\alpha(\boldsymbol{x}+\boldsymbol{e}_i\delta_t, t+\delta_t)]. \tag{2.50}$$

### 2.6.2   Fluid flow parameters

The Mach number is the ratio between the fluid speed and speed of sound, or

$$Ma = \frac{u}{c_s}. \tag{2.51}$$

Laminar flows in porous media usually have a very low Mach number. However, in lattice Boltzmann simulations, the artificially low $c_s$ described in Section 2.6.3 can raise simulated Mach number by a large factor.

The Reynolds number of a fluid is given as

$$Re = \frac{UL}{\nu}, \tag{2.52}$$

where $U$ and $L$ are the characteristic velocity and length, and $\nu$ is the kinematic viscosity.

The Knudsen number is defined as

$$Kn = \frac{L_{mfp}}{L_M} = \frac{Ma}{Re}, \tag{2.53}$$

where $Ma$ is the Mach number, $L_{mfp}$ is the mean free path between collisions and $L_M$ is the macroscopic length scale of the flow.

In the LBGK scheme, $\tau$ is directly related to viscosity through the relation given in equation (2.61). In principle, this relationship gives us the possibility to select any viscosity by choosing $\tau$ between 0.5 (no viscosity) and $\infty$ (infinite viscosity, in effect an extremely high velocity solid). However, in practice, the selection is more limited.

In practice, we are often interested in simulating flows with a high Reynolds number, which will indicate a $\tau \approx 0.5$. Unfortunately, simulations with this relaxation parameter are often unstable. This can be explained partially by the high Mach numbers associated with low viscosities. He *et. al.* [47] also identified the uniform mesh as a cause for trouble, and worked to remedy the problem by introducing a nonuniform grid.

Any $\tau < 1$ is an overrelaxation scheme, where the distribution function not only approaches, but surpasses the equilibrium distribution during the collision step. This corresponds to high Reynolds flows, and are useful when modelling turbulence. A risk with such models is that the realizability constraint

$$f_i > 0, \tag{2.54}$$

may be violated if the Mach number is large, or if the initial distribution is far from equilibrium, although this is usually not a concern for low-Mach flows.

The situation with $\tau = 1$ has been called the safest choice by Sukop and Thorne [48]. This parameter indicates immediate relaxation to the equilibrium, and carries none of the dangers of over-relaxation schemes. Computationally, $\tau = 1$ is efficient because it simply involves calculating the equilibrium distribution and using that for the post-relaxation distribution. Finding the post-relaxation distribution for other values of $\tau$ involves an additional calculation for a distribution between the pre-collision and equilibrium distributions (for $\tau > 1$) or beyond the equilibrium distribution (for $\tau < 1$) [25]. However, $\tau = 1$ can also correspond to an undesirably low Reynolds number

### 2.6.3  Adapting the speed of sound

In the lattice Boltzmann method, the speed of sound $c_s = 1/\sqrt{3}$ measured in lattice units. In a real fluid, the speed of sound is typically in the order of 1000 m/s, if the lattice spacing $\delta_x$ is small, converting this directly to lattice units requires us to choose a very small time step $\delta_t$. Typically, such a conversion will also force us to select a relaxation parameter very close to 0.5 in order to maintain the correct viscosity, an overrelaxation scheme which can severely endanger the stability of our simulations.

It is usual to adapt to this problem by letting the Mach number of our simulated fluids far exceed the real one ([23], Section 8.3). In order to preserve the Reynolds number, we increase the viscosity $v$ by the same factor as we increase the Mach number. For small scale problems, this has the added benefit of bringing the relaxation parameter $\tau$ closer to 1, which results in a more stable simulation. This adaptive increase the Mach number is in effect a reduction of the speed of sound.

A consequence of this adaption is that the Knudsen number, defined in equation (2.53), is increased. Consequently, our aim to maintain fluid flow relies on an assumption that proper hydrodynamics can be achieved in only a few mean free paths. Numerical experiments have shown that as long as $Kn > 0.01$, this approach is viable [23]. If the Knudsen number is in the range $0.01 < Kn < 0.1$, we have a slip-flow regime, where there may be a nonzero velocity at the walls even though the Navier-Stokes equation is still usable. For $0.1 < Kn < 3$, a transition regime arises where the Navier-Stokes equation loses its applicability [49].

### 2.6.4  Pressure

In the lattice Boltzmann method described here, the pressure $p$ in single-phase regions is calculated using the ideal gas equation. The familiar form of this equation for gas in an enclosed box of volume $V$ is

$$pV = n_m RT, \tag{2.55}$$

where $n_m$ is the number of moles, $R = 8.314$ J/mol K is the ideal gas constant and $T$ is the absolute temperature, or

$$pV = NkT, \tag{2.56}$$

where $N$ is the number of molecules and $k = 1.381 \times 10^{-23}$ J/K is Boltzmann's constant. Avogadro's constant is given by the ratios $\frac{N}{n}$ or $\frac{R}{k}$.

In the dimensionless lattice Boltzmann model, the ideal gas equation is given by

$$p = c_s^2 \rho, \tag{2.57}$$

where $\rho$ is the particle density, and $c_s = \sqrt{RT}$ is the speed of sound. In the D2Q9 and D3Q27 models, $c_s^2 = \frac{c^2}{3}$ [34].

For the isothermal models ($T$ constant), any pressure variations must be attributed to variations in particle density. This does violate the incompressibility assumption of liquids, but the density variations are generally small, $O(Ma^2)$.

The ideal gas equation is valid for rarefied gases, and using the equation to measure the pressure in incompressible liquids may seem counterintuitive. The justification for this is that the Knudsen number (2.53) in the simulations is several orders of magnitude larger than the Knudsen number in a real liquid, in particular the mean free path between molecules is greatly exaggerated in the lattice Boltzmann simulation. Consequently, the simulated fluid behaves more like a gas than the real and incompressible liquids.

Some of the two-phase flow methods, in particular the Shan-Chen method described in Section 3.2 and Enskog-based method in Section 3.3.2, involve large internal forces, and require additional nonideal pressure terms in interfacial regions.

### 2.6.5 Converting to and from physical units

Conversion between lattice units and physical units is essential if we are dealing with a physical problem. In principle, we would like the conversion to preserve the Reynold's number, Knudsen number, as well as the correct length, time, and macroscopic velocity, though we will see that fulfilling all these criteria is not always possible or desirable. In order to obtain qualitatively correct simulations, the priority is to preserve the correct length and time scales as well as the Reynold's number (equation 2.52) which should be calculated beforehand. Conversions are covered by Succi [23], appendix D.

**Length**

Discretizing a domain of size $M \times N$, into an $m \times n$ lattice is fairly straightforward. In the D2Q9 model, the cells need to be square, not rectangular so the ratio

between the length and width of the physical and lattice domains must be equal, $M/N = m/n$. The size of the spatial lattice unit $\delta_x$ is given by

$$\delta_x = \frac{M}{m} = \frac{N}{n},$$
(2.58)

where the unit for $\delta_x$ is the same as for $M$.

**Time**

The time step $\delta t$ is given by

$$\delta_t = \frac{\delta_x}{c_s},$$
(2.59)

where $c_s$ is the *fictitious* speed of sound. If we are modelling fluid flow on the small pore scale, this is generally much smaller than the real speed of sound as discussed in Section 2.6.3.

**Viscosity**

With the space and time steps defined, the kinematic lattice viscosity $\nu_L$ can be calculated:

$$\nu_L = \nu \frac{\delta_t}{\delta_x^2},$$
(2.60)

where $\nu$ is the physical kinematic viscosity, albeit scaled up as described in Section 2.6.3. Note that while $\nu$, $\delta_x$, and $\delta_t$ have dimensions $m^2/s$, $m$, and $s$ respectively, $\nu_L$ is dimensionless.

The viscosity of the fluid $\nu_L$ is dependent on the relaxation time $\tau$ and with $c = 1$ given by

$$\nu_L = \frac{2\tau - 1}{6},$$
(2.61)

this allows $\tau$ to be calculated. Equation (2.61) comes from the Chapman-Enskog expansion of the LBGK equation, covered in Section 2.7.

## 2.7 Chapman-Enskog expansion

The connection between the Boltzmann equation (2.6) and the classical equations (1.1)–(1.5) for fluid flow was found by Enskog. It was published in the classical work by Chapman and Cowling [36] and is known as the Chapman-Enskog expansion. The method involves a perturbation expansion of the distribution function using the Knudsen number, defined in equation (2.53), as the expansion parameter $\epsilon$. The idea is to obtain fluid equations on the local $\epsilon$ scale and the larger $\epsilon^2$ scale.

The presentation of this expansion varies somewhat in the literature, and depends on which equation (e.g. Boltzmann, lattice Boltzmann, LBGK, etc.) is being expanded. The presentation here is based on the one given by Wolf-Gladrow [25], Section 5.2.3, for the D2Q9 LBGK model.

The distribution function $f$ is expanded through

$$f_i(\boldsymbol{x}, t) = f_i^{(0)} + \epsilon f_i^{(1)} + \epsilon^2 f_i^{(2)} + O(\epsilon^3), \tag{2.62}$$

where the $f_i^{(0)}$ term is the local equilibrium distribution function $f_i^{eq}$ and accounts for the density and momentum. The nonequilibrium terms $f_i^{(1)}$ and $f_i^{(2)}$ do not contribute to these moments, that is:

$$\sum_i f_i^{(n)} = \begin{cases} \rho, & n = 0 \\ 0, & n > 0 \end{cases} \tag{2.63}$$

$$\sum_i f_i^{(n)} \boldsymbol{e}_i = \begin{cases} \rho\boldsymbol{u}, & n = 0 \\ 0, & n > 0 \end{cases} \tag{2.64}$$

The expansion operates on two time scales (a fast sound wave time scale and a slow diffusion time scale), while space is expanded on a single scale. Hence, the differential operators with respect to time and space are given by:

$$\frac{\partial}{\partial t} = \epsilon \frac{\partial}{\partial t^{(1)}} + \epsilon^2 \frac{\partial}{\partial t^{(2)}}, \tag{2.65}$$

$$\frac{\partial}{\partial x_\alpha} = \epsilon \frac{\partial}{\partial x_\alpha}, \tag{2.66}$$

$$\tag{2.67}$$

and the first and second order derivatives of the distribution function are therefore

$$\frac{\partial f_i}{\partial t} = \epsilon \frac{\partial f_i^{(0)}}{\partial t^{(1)}} + \epsilon^2 \left( \frac{\partial f_i^{(0)}}{\partial t^{(2)}} + \frac{\partial f_i^{(1)}}{\partial t^{(1)}}, \right) + O(\epsilon^3), \tag{2.68}$$

$$\frac{\partial f_i}{\partial x_\alpha} = \epsilon \frac{\partial f_i^{(0)}}{\partial x_\alpha} + \epsilon^2 \frac{\partial f_i^{(1)}}{\partial x_\alpha^{(1)}} + O(\epsilon^3), \tag{2.69}$$

$$\frac{\partial^2 f_i}{\partial t^2} = \epsilon^2 \frac{\partial^2 f_i^{(0)}}{[\partial t^{(1)}]^2} + O(\epsilon^3), \tag{2.70}$$

$$\frac{\partial^2 f_i}{\partial t \partial x_\alpha} = \epsilon^2 \frac{\partial^2 f_i^{(0)}}{\partial t^{(1)} \partial x_\alpha^{(1)}} + O(\epsilon^3), \tag{2.71}$$

$$\frac{\partial^2 f_i}{\partial x_\alpha^2} = \epsilon^2 \frac{\partial^2 f_i^{(0)}}{[\partial x_\alpha^{(1)}]^2} + O(\epsilon^3). \tag{2.72}$$

With external forces $\boldsymbol{F}$, we recall from equation (2.50) that the Lattice BGK equation is given by

$$f_i(\boldsymbol{x}+\boldsymbol{e}_i\delta_t,t+\delta_t)-f_i(\boldsymbol{x},t)=-\frac{\delta_t}{\tau}(f_i-f_i^{eq})+\frac{\delta_t e_{\alpha i}}{12c^2}[F_\alpha(\boldsymbol{x},t)+F_\alpha(\boldsymbol{x}+\boldsymbol{e}_i\delta_t,t+\delta_t)].$$

The terms $f_i(\boldsymbol{x}+\boldsymbol{e}_i\delta_t,t+\delta_t)$ and $F_\alpha(\boldsymbol{x}+\boldsymbol{e}_i,t+\delta_t)$ are expanded in a Taylor series, with the result:

$$
\begin{aligned}
0 \;=\;& \delta_t\frac{\partial f_i}{\partial t}+\delta_t e_{i\alpha}\frac{\partial f_i}{\partial x_\alpha}+\frac{\delta_t^2}{2}\left(\frac{\partial^2 f_i}{\partial t^2}+2e_{i\alpha}\frac{\partial^2 f_i}{\partial x_\alpha \partial t}+e_{i\alpha}e_{i\beta}\frac{\partial^2 f_i}{\partial x_\alpha \partial x_\beta}\right)\\
&+O(\partial^3 f)+\frac{\delta_t}{\tau}(f_i(\boldsymbol{x},t)-f_i^{eq}(\boldsymbol{x},t))\\
&-\frac{\delta_t e_{i\alpha}}{6c^2}F_\alpha-\frac{\delta_t^2}{c^2}\frac{e_{i\alpha}}{12}\left(\frac{\partial F_\alpha}{\partial t}+e_{i\beta}\frac{\partial F_\alpha}{\partial x_\beta}\right)+O(\delta_t^3).
\end{aligned}
\tag{2.73}
$$

The expansion of $f$ and its derivatives (equations 2.62 and 2.68–2.72) is now inserted along with the expanded derivatives of $\boldsymbol{F}$ into equation (2.73) to obtain terms on the $\epsilon$ and $\epsilon^2$ scales.

$$
\begin{aligned}
0 \;=\;& \delta_t\left[\epsilon\frac{\partial f_i^{(0)}}{\partial t^{(1)}}+\epsilon^2\left(\frac{\partial f_i^{(0)}}{\partial t^{(2)}}+\frac{\partial f_i^{(1)}}{\partial t^{(1)}}\right)\right]+\delta_t e_{i\alpha}\left(\epsilon\frac{\partial f_i^{(0)}}{\partial x_\alpha^{(1)}}+\epsilon^2\frac{\partial f_i^{(1)}}{\partial x_\alpha^{(1)}}\right)\\
&+\frac{\delta_t^2}{2}\epsilon^2\left(\frac{\partial^2 f_i^{(0)}}{[\partial t^{(1)}]^2}+2e_{i\alpha}\frac{\partial^2 f_i^{(0)}}{\partial t^{(1)}\partial x_\alpha^{(1)}}+e_{i\alpha}e_{i\beta}\frac{\partial^2 f_i^{(0)}}{[\partial x_\alpha^{(1)}]^2}\right)\\
&+\frac{\delta_t}{\tau}(\epsilon f_i^{(1)}+\epsilon^2 f_i^{(2)})-\frac{\delta_t}{c^2}\frac{e_{i\alpha}}{6}F_\alpha\\
&-\frac{\delta_t^2}{c^2}\frac{e_{i\alpha}}{12}\left[\epsilon\left(\frac{\partial F_\alpha}{\partial t^{(1)}}+e_{i\beta}\frac{\partial F_\alpha}{\partial x_\beta^{(1)}}\right)+\epsilon^2\frac{\partial F_\alpha}{\partial t^{(2)}}\right]+O(\epsilon^3),
\end{aligned}
\tag{2.74}
$$

if we also assume that the external forces act on the $\epsilon$-scale, so that $\boldsymbol{F}=\epsilon\boldsymbol{G}$, we can eliminate the last $\epsilon^0$-terms in equation (2.74)

$$
\begin{aligned}
0 \;=\;& \delta_t\left[\epsilon\frac{\partial f_i^{(0)}}{\partial t^{(1)}}+\epsilon^2\left(\frac{\partial f_i^{(0)}}{\partial t^{(2)}}+\frac{\partial f_i^{(1)}}{\partial t^{(1)}}\right)\right]+\delta_t e_{i\alpha}\left(\epsilon\frac{\partial f_i^{(0)}}{\partial x_\alpha^{(1)}}+\epsilon^2\frac{\partial f_i^{(1)}}{\partial x_\alpha^{(1)}}\right)\\
&+\frac{\delta_t^2}{2}\epsilon^2\left(\frac{\partial^2 f_i^{(0)}}{[\partial t^{(1)}]^2}+2e_{i\alpha}\frac{\partial^2 f_i^{(0)}}{\partial t^{(1)}\partial x_\alpha^{(1)}}+e_{i\alpha}e_{i\beta}\frac{\partial^2 f_i^{(0)}}{[\partial x_\alpha^{(1)}]^2}\right)\\
&+\frac{\delta_t}{\tau}(\epsilon f_i^{(1)}+\epsilon^2 f_i^{(2)})-\epsilon\frac{\delta_t}{c^2}\frac{e_{i\alpha}}{6}G_\alpha\\
&-\epsilon^2\frac{\delta_t^2}{c^2}\frac{e_{i\alpha}}{12}\left(\frac{\partial G_\alpha}{\partial t^{(1)}}+e_{i\beta}\frac{\partial G_\alpha}{\partial x_\beta^{(1)}}\right)+O(\epsilon^3),
\end{aligned}
\tag{2.75}
$$

### 2.7.1  Terms of $O(\epsilon)$

The first fluid equations can be found at the short $\epsilon$ scale. The $\epsilon$ terms in equation (2.75) are given by:

$$0 = \delta_t \left( \frac{\partial f_i^{(0)}}{\partial t^{(1)}} + e_{i\alpha} \frac{\partial f_i^{(0)}}{\partial x_\alpha^{(1)}} + \frac{1}{\tau} f_i^{(1)} - \frac{1}{c^2} \frac{e_{i\alpha}}{6} G_\alpha \right) \qquad (2.76)$$

**The zeroth moment**

Taking the zeroth moment of (2.76), and recalling the moments in equation (2.63) gives the equation

$$\frac{\partial \rho}{\partial t^{(1)}} + \frac{\partial}{\partial x_\alpha}(\rho u_\alpha) = \frac{\partial \rho}{\partial t^{(1)}} + \nabla \cdot (\rho u) = 0, \qquad (2.77)$$

which we recognize as the continuity equation (1.1) on the short time scale $t^{(1)}$.

**The $e_i$-moment**

If we take the first moment of (2.76), we obtain

$$0 = \sum_i e_{i\beta} \left[ \frac{\partial f_i^{(0)}}{\partial t^{(1)}} + e_{i\alpha} \frac{\partial f_i^{(0)}}{\partial x_\alpha^{(1)}} + \frac{1}{\tau} f_i^{(1)} - \frac{\delta_t}{c^2} \frac{e_{i\alpha}}{6} G_\alpha \right]. \qquad (2.78)$$

Three of these terms are easy to process. The first term is the definition of momentum as seen in equation (2.63). The third term is a moment over a the non-equilibrium distribution term $f^{(1)}$ and therefore zero. For the fourth term, note that

$$\sum_i e_{i\alpha} e_{i\beta} = 6c^2 I, \qquad (2.79)$$

where $I$ is the identity matrix, and that this term is therefore simply $G_\alpha$.

The more complex second term may be written as $\frac{\partial}{\partial x_\alpha} P_{\alpha\beta}^{(0)}$, where $P_{\alpha\beta}^{(0)}$ is a momentum flux matrix defined as

$$P_{\alpha\beta}^{(0)} = \sum_i c_{i\alpha} c_{i\beta} F_i^{(0)} = \frac{1}{\rho} \begin{pmatrix} \rho^2 u_1^2 & \rho^2 u_1 u_2 \\ \rho^2 u_1 u_2 & \rho^2 u_2^2 \end{pmatrix} + \frac{kT}{m} \rho I, \qquad (2.80)$$

where the last term is the ideal pressure $p$.

The moment (2.78) is thus equal to

$$\frac{\partial u}{\partial t^{(1)}} + u \nabla u + \frac{1}{\rho} \nabla p - G = 0, \qquad (2.81)$$

which is the Euler equation (1.5).

## 2.7.2 Terms of $O(\epsilon^2)$

The terms on the longer $\epsilon^2$ scale from equation (2.75) are given by:

$$
\begin{aligned}
0 \;=\; \delta_t \Bigg[ & \frac{\partial f_i^{(1)}}{\partial t^{(1)}} + \frac{\partial f_i^{(0)}}{\partial t^{(2)}} + e_{i\alpha}\frac{\partial f_i^{(1)}}{\partial x_\alpha^{(1)}} + \frac{\delta_t}{2}\frac{\partial^2 f_i^{(0)}}{[\partial t^{(1)}]^2} + \delta_t e_{i\alpha}\frac{\partial^2 f_i^{(0)}}{\partial x_\alpha^{(1)}\partial t^{(1)}} \\
& + \frac{\delta_t}{2} e_{i\alpha} e_{i\beta}\frac{\partial^2 f_i^{(0)}}{\partial x_\alpha^{(1)}\partial x_\beta^{(1)}} + \frac{1}{\tau} f_i^{(2)} - \frac{\delta_t e_{i\alpha}}{12c^2}\frac{\partial G_\alpha}{\partial t^{(1)}} - \frac{\delta_t e_{i\alpha} e_{i\beta}}{12c^2}\frac{\partial G_\alpha}{\partial x_\beta^{(1)}} \Bigg] \quad (2.82)
\end{aligned}
$$

**The zeroth moment**

Taking the zeroth order moment of (2.82) and dividing by $\delta_t$ gives

$$
\begin{aligned}
0 \;=\; \sum_i \Bigg[ & \frac{\partial f_i^{(1)}}{\partial t^{(1)}} + \frac{\partial f_i^{(0)}}{\partial t^{(2)}} + e_{i\alpha}\frac{\partial f_i^{(1)}}{\partial x_\alpha^{(1)}} + \frac{\delta_t}{2}\frac{\partial^2 f_i^{(0)}}{[\partial t^{(1)}]^2} + \delta_t e_{i\alpha}\frac{\partial^2 f_i^{(0)}}{\partial x_\alpha^{(1)}\partial t^{(1)}} \\
& + \frac{\delta_t}{2} e_{i\alpha} e_{i\beta}\frac{\partial^2 f_i^{(0)}}{\partial x_\alpha^{(1)}\partial x_\beta^{(1)}} + \frac{1}{\tau} f_i^{(2)} - \frac{\delta_t e_{i\alpha}}{12c^2}\frac{\partial G_\alpha}{\partial t^{(1)}} - \frac{\delta_t e_{i\alpha} e_{i\beta}}{12c^2}\frac{\partial G_\alpha}{\partial x_\beta^{(1)}} \Bigg] \quad (2.83)
\end{aligned}
$$

Since the first, third, and seventh terms are first order moments over non-equilibrium terms, these vanish in accordance with equation (2.63). The eighth term is also zero since it can be written as $\frac{\delta_t}{12c^2}\frac{\partial G_\alpha}{\partial t^{(1)}}\sum_i c_{i\alpha}$ and the sum of all discrete velocities is zero. When summed over $i$, the second term becomes $\frac{\partial\rho}{\partial t^{(2)}}$, while using (2.79) shows that the last term is equal to $-\frac{\delta_t}{2}\frac{\partial G_\alpha}{\partial x_\alpha^{(1)}}$. The fourth term can be written as $\frac{\delta_t}{2}\frac{\partial}{\partial t^{(1)}}(\frac{\partial\rho}{\partial t^{(1)}})$, and using the continuity equation (2.77) followed by equation (2.78) we can write

$$
\begin{aligned}
\sum_i \frac{\delta_t}{2}\frac{\partial}{\partial t^{(1)}}\left[\frac{\partial\rho}{\partial t^{(1)}}\right] \;&=\; -\frac{\delta_t}{2}\frac{\partial}{\partial x_\beta^{(1)}}\left[\frac{\partial(\rho u_\beta)}{\partial t^{(1)}}\right] \\
&=\; -\frac{\delta_t}{2}\frac{\partial}{\partial x_\beta^{(1)}}\left[-\frac{\partial P_{\alpha\beta}^{(0)}}{\partial x_\beta^{(0)}} + G_\beta\right] \\
&=\; \frac{\delta_t}{2}\frac{\partial^2}{\partial x_\alpha^{(1)}\partial x_\beta^{(1)}}(P_{\alpha\beta}^{(0)}) - \frac{\delta_t}{2}\frac{\partial G_\alpha}{\partial x_\alpha^{(1)}}. \quad (2.84)
\end{aligned}
$$

In similar fashion, the fifth and sixth terms in equation (2.83) can be written as

$$\sum_i \delta_t e_{i\alpha} \frac{\partial^2 f_i^{(0)}}{\partial x_\alpha^{(1)} \partial t^{(1)}} = -\delta_t \frac{\partial^2}{\partial x_\alpha^{(1)} \partial x_\beta^{(1)}}(P_{\alpha\beta}^{(0)}) + \delta_t \frac{\partial G_\alpha}{\partial x_\alpha^{(1)}} \qquad (2.85)$$

$$\sum_i \frac{\delta_t}{2} e_{i\alpha} e_{i\beta} \frac{\partial^2 f_i^{(0)}}{\partial x_\alpha^{(1)} \partial x_\beta^{(1)}} = \frac{\delta_t}{2} \frac{\partial^2}{\partial x_\alpha^{(1)} \partial x_\beta^{(1)}}(P_{\alpha\beta}^{(0)}). \qquad (2.86)$$

Thus the sum of the fourth, fifth, and sixth terms is given by $\frac{\delta_t}{2}\frac{\partial G_\alpha}{\partial x_\alpha^{(1)}}$, cancelling out the last term in equation (2.83). What remains is the incompressibility condition at the long $t^{(2)}$ scale

$$\frac{\partial \rho}{\partial t^{(2)}} = 0. \qquad (2.87)$$

### The $e_i$-moment

The $\boldsymbol{e}_i$-moment of (2.82) gives the following expression after dividing through by $\delta_t$:

$$\begin{aligned}
0 = \sum_i &\left[ e_{i\alpha} \frac{\partial f_i^{(1)}}{\partial t^{(1)}} + e_{i\alpha} \frac{\partial f_i^{(0)}}{\partial t^{(2)}} + e_{i\alpha} e_{i\beta} \frac{\partial f_i^{(1)}}{\partial x_\beta^{(1)}} + \frac{\delta_t}{2} e_{i\alpha} \frac{\partial^2 f_i^{(0)}}{[\partial t^{(1)}]^2} \right. \\
&+ \delta_t e_{i\alpha} e_{i\beta} \frac{\partial^2 f_i^{(0)}}{\partial x_\beta^{(1)} \partial t^{(1)}} + \frac{\delta_t}{2} e_{i\alpha} e_{i\beta} e_{i\gamma} \frac{\partial^2 f_i^{(0)}}{\partial x_\beta^{(1)} \partial x_\gamma^{(1)}} + \frac{1}{\tau} e_{i\alpha} f_i^{(2)} \\
&\left. - \frac{\delta_t e_{i\alpha} e_{i\beta}}{12 c^2} \frac{\partial G_\beta}{\partial t^{(1)}} - \frac{\delta_t e_{i\alpha} e_{i\beta} e_{i\gamma}}{12 c^2} \frac{\partial G_\gamma}{\partial x_\beta^{(1)}} \right]
\end{aligned} \qquad (2.88)$$

In this case, the first and seventh terms are first order moments over nonequilibrium distribution terms, and vanish in accordance with equation (2.63). The ninth term also vanishes since it can be written $-\frac{\delta_t}{12c^2}\frac{\partial G_\gamma}{\partial x_\beta^{(1)}}\sum_i e_{i\alpha}e_{i\beta}e_{i\gamma}$, where the sum is zero. We recognize the second term as

$$\sum_i e_{i\alpha} \frac{\partial f_i^{(0)}}{\partial t^{(2)}} = \frac{\partial(\rho\boldsymbol{u})}{\partial t^{(2)}}. \qquad (2.89)$$

The third term involves a moment over the nonequilibrium $f^{(1)}$, but since it is of second order this does *not* vanish and we need to account for $f_i^{(1)}$ terms this time.

According to equation (2.76), $f_i^{(1)}$ is given by

$$f_i^{(1)} = -\tau \frac{\partial f_i^{(0)}}{\partial t^{(1)}} - \tau e_{i\alpha} \frac{\partial f_i^{(0)}}{\partial x_\alpha^{(1)}} + \frac{\tau}{c^2} \frac{e_{i\alpha}}{6} G_\alpha, \tag{2.90}$$

so writing out the third term of (2.88) in terms of $f_i^{(0)}$ we obtain

$$
\begin{aligned}
e_{i\alpha} e_{i\beta} \frac{\partial f_i^{(1)}}{\partial x_\beta^{(1)}} &= -\tau \frac{\partial^2}{\partial t^{(1)} \partial x_\beta^{(1)}} \left[ \sum_i e_{i\alpha} e_{i\beta} f_i^{(0)} \right] - \tau \frac{\partial^2}{\partial x_\alpha^{(1)} \partial x_\beta^{(1)}} \left[ e_{i\alpha} e_{i\beta} e_{i\gamma} f_i^{(0)} \right] \\
&\quad + \frac{1}{6c^2\tau} \frac{\partial G_\alpha}{\partial x_\beta} \sum_i e_{i\alpha} e_{i\beta} e_{i\gamma},
\end{aligned}
\tag{2.91}
$$

where the last term is zero since $\sum_i e_{i\alpha} e_{i\beta} e_{i\gamma} = 0$. We recognize that the fifth and sixth terms of equation (2.88) are of the same type as the first two terms in (2.91). The fourth term can be written as

$$
\begin{aligned}
\frac{\delta_t}{2} e_{i\alpha} \frac{\partial^2 f_i^{(0)}}{[\partial t^{(1)}]^2} &= \frac{\delta_t}{2} \frac{\partial}{\partial t^{(1)}} \left[ \frac{\partial}{\partial t^{(1)}} (\rho \boldsymbol{u}) \right] \\
&= \frac{\delta_t}{2} \frac{\partial}{\partial t^{(1)}} \left[ -\frac{\partial}{\partial x_\beta^{(1)}} P_{\alpha\beta}^{(0)} + G_\alpha \right] \\
&= \frac{\delta_t}{2} \frac{\partial}{\partial t^{(1)}} \left[ -\frac{\partial}{\partial x_\beta^{(1)}} \left( \frac{kT}{m} \rho I \right) + G_\alpha + O((\rho \boldsymbol{u})^2) \right]
\end{aligned}
\tag{2.92}
$$

where the second equality is due to equation (2.76). The derivation of the Navier-Stokes equation neglects the $O(\rho \boldsymbol{u})^2$ terms and is thus valid for a low Mach number only. The eighth term can be written as

$$
\begin{aligned}
-\frac{\delta_t e_{i\alpha} e_{i\beta}}{12c^2} \frac{\partial G_\alpha}{\partial t^{(1)}} &= -\frac{\delta_t}{12c^2} \frac{\partial G_\alpha}{\partial t^{(1)}} \sum_i e_{i\alpha} e_{i\beta} \\
&= -\frac{\delta_t}{2} \frac{\partial G_\alpha}{\partial t^{(1)}}
\end{aligned}
\tag{2.93}
$$

where equation (2.79) has been used. Note that this term cancels the external force term in equation (2.92).

Adding the first term of equation (2.91) with the fifth term in equation (2.88) obtains

$$
\begin{aligned}
(\delta_t - \tau) \frac{\partial^2}{\partial x_\beta^{(1)} \partial t^{(1)}} \sum_i e_{i\alpha} e_{i\beta} f_i^{(0)} &\approx -(\delta_t - \tau) \frac{\partial^2}{\partial x_\beta^{(1)} \partial t^{(1)}} \frac{kT}{m} \rho I \\
&= -(\delta_t - \tau) \frac{kT}{m} \nabla \nabla \cdot (\rho \boldsymbol{u}),
\end{aligned}
\tag{2.94}
$$

where the approximation again neglects terms of $O((\rho\boldsymbol{u})^2)$. Similarly, the second term of equation (2.91) plus the sixth term of equation (2.88) yields the term

$$\left(\frac{\delta_t - 2\tau}{2}\right)\frac{\partial^2}{\partial x_\alpha^{(1)}\partial x_\beta^{(1)}}\sum_i e_{i\alpha}e_{i\beta}e_{i\gamma}f_i^{(0)} = \left(\frac{\delta_t - 2\tau}{2}\right)\frac{kT}{m}(\nabla^2(\rho\boldsymbol{u}) + \nabla\nabla\cdot(\rho\boldsymbol{u}))$$

(2.95)

Adding together equations (2.89), (2.92), (2.93), (2.94, and (2.95)) yields the equation

$$\frac{\partial(\rho\boldsymbol{u})}{\partial t^{(2)}} = (\tau - \frac{\delta_t}{2})\frac{kT}{m}(\nabla\nabla\cdot(\rho\boldsymbol{u})).$$

(2.96)

Combining equations (2.87), (2.87), and (2.96) gives the incompressible continuity equation

$$\nabla\cdot\boldsymbol{u} = 0,$$

(2.97)

and the Navier-Stokes equation

$$\frac{\partial\boldsymbol{u}}{\partial t} + (\boldsymbol{u}\nabla)\boldsymbol{u} = -\frac{1}{\rho}\nabla p + \nu\nabla^2\boldsymbol{u} + \boldsymbol{G}$$

(2.98)

where $\nu$ is given by

$$\nu = c^2\left(\frac{2\tau - 1}{6}\right)$$

(2.99)

Most lattice Boltzmann simulations normalize the discrete speed so that $c = 1$.

# Chapter 3

# Phase and component flow

When discussing lattice Boltzmann simulations for multiphase flow, we need to distinguish between two broad categories. In some cases the particles in each of the phases are the same, for example water-vapor systems. These are called single-component multiphase (SCMP) systems. In other cases the different phases feature different particles, such as oil-water systems. These are called multi-component multiphase (MCMP) systems. The MCMP models are of particular interest because of their use in modelling flows in oil and gas reservoirs [48].

Multiphase flow has been implemented in numerous ways, several of these are summarized by Succi [23]. This chapter contains some detail about the most popular models, and a brief description of some additional ones. In our work we have concentrated on multi-component multiphase flows such as oil and water. Some of the models can, with some modification, also handle multiphase flows with a single component, such as water and water vapor.

## 3.1   Color model

The first effective method for multiphase flows was the so called "chromody-namic", or "color" model. The method was introduced by Gunstensen *et. al.* [50]. This model was based on the multiphase Lattice-Gas model of Rothman and Keller [51]. Although it is the oldest model, interest in it persists, and there are several fairly recent improvements to the chromodynamic model, e.g. Reis and Phillips [52], Wu *et al.* [53], and Tölke *et al.* [54], the last of which includes MRT implementation.

The model is designed for a two-phase, two-component system. In this model, both of the phases are designated by a different "color", for example red and blue. The "color" is a placeholder term to generalise different components, for example in an oil water system we could let "red" represent oil and "blue" represent wa-

ter. Both components have a separate distribution function, denoted $f_i^R$ and $f_i^B$, with the superscripts representing the red and blue components respectively. An arbitrary phase is designated with the superscript $a$.

The color difference $\Delta\rho$ is defined by

$$\Delta\rho = \rho^R - \rho^B. \tag{3.1}$$

Each of the populations follow a regular propagation step

$$f^a(\boldsymbol{x} + \boldsymbol{e}_i, t+1) = f_i^a, \tag{3.2}$$

but the collision step contains additional terms to the standard BGK operator in order to produce surface tension and phase separation.

Central to the chromodynamic model are the concepts of color gradient $\boldsymbol{G}$, which is simply defined as $\nabla(\Delta\rho)$, but can be approximated (in the D2Q9 lattice) to the fourth order by [52]

$$\boldsymbol{G}(\boldsymbol{x}) \approx \sum_{i=1}^{8} c_i \Delta\rho(\boldsymbol{x} + \boldsymbol{c}_i), \tag{3.3}$$

and the color flux $\boldsymbol{K}$

$$\boldsymbol{K}(\boldsymbol{x}) = \sum_{i=1}^{8} (f_i^R - f_i^B) \boldsymbol{e}_i. \tag{3.4}$$

The generation of surface tension and segregation of phases are handled in two different processes by adding additional terms to the collision operator $\Omega$. In literature on the color models, different methods and algorithms are proposed. A common characteristic is that the collision term $\Omega$ consists of three parts which can be written as [55]

$$\Omega_i^a = \Omega 3_i^a [\Omega 1_i^a + \Omega 2_i^a], \tag{3.5}$$

where $\Omega 1_i^a$ is the standard BGK operator, surface tension is generated through the source term $\Omega 2_i^a$, and phase separation is handled by $\Omega 3_i^a$.

The original color model was made for a hexagonal lattice, and $\Omega_2$ was then given by (see for example Grunau et al. [56]) by

$$\Omega 2_i^a = \frac{A}{2} |\boldsymbol{G}| \left( \frac{(\boldsymbol{e}_i \cdot \boldsymbol{G})^2}{G^2} - \frac{1}{2} \right). \tag{3.6}$$

A straightforward extension of the model to the D2Q9 lattice would give

$$\Omega 2_i^a = \frac{A}{2} |\boldsymbol{G}| \left( \frac{(\boldsymbol{e}_i \cdot \boldsymbol{G})^2}{G^2} - \frac{3}{4} \right), \qquad i = 1 \ldots 8, \tag{3.7}$$

however Reis and Phillips [52] observed that equation (3.7) would not yield the correct stress tensor for the square lattice. Instead, they proposed some different parameters for the operator, giving it as

$$\Omega 2_i^a = \frac{A}{2}|\boldsymbol{G}|\left(w_i\frac{(\boldsymbol{e}_i \cdot \boldsymbol{G})^2}{\boldsymbol{G}^2} - B_i\right), \qquad i = 0\ldots 8, \tag{3.8}$$

where $B_i$ is given by

$$B_i = \begin{cases} -4/27, & i = 0, \\ 2/27, & i = 1, 2, 3, 4 \\ 5/108, & i = 5, 6, 7, 8. \end{cases}, \tag{3.9}$$

and showed that the formulation given by (3.8) yields the correct interfacial stress tensor when the Chapman-Enskog technique is applied.

While $\Omega 2_i^a$ generates surface tension, it does not prevent components from mixing. For phase segregation, a recoloring step is applied through the $\Omega 3_i^a$ term. As with $\Omega 2_i^a$, there have been different proposals regarding how $\Omega 3_i^a$ should be designed. The common aim involves solving the maximisation problem

$$W(f^R, f^B) = \max_{f^R, f^B}\left[\sum_i (f^R - f^B)\boldsymbol{e}_i\right] \cdot \boldsymbol{G}, \tag{3.10}$$

under the constraints of conservation of mass of each component and conservation of total momentum.

The total number of red and blue particles is conserved on each lattice vector $\boldsymbol{e}_i$, ensuring conservation of momentum. For conservation of mass, the total number of red particles, and the total of blue particles, is conserved at each node. Hence, the effect of the operator is to have some of the red and blue particles trade places with each other.

Gunstensen *et al.* [50] point out that the presence of rest particles allows for thin one-node wide interfaces, because the rest particles can handle the fluid mixture. Without rest particles, the recoloring may be forced to assign excess particles in the wrong direction, which increases the interface thickness.

One simple method is to sort all the lattice vectors starting with the one closest to the color gradient. In the case of a D2Q9 lattice with 8 nonzero velocity vectors, there are sixteen possible configurations, covered in table 3.1.

Red particles are then assigned to each of the lattice vectors, starting with the one closest to the color gradient. If this makes all the particles on that vector "red", further red particles that need to be accounted for are added to the second closest vector until this is filled, and so on. Once all red particles in the node have been assigned to a vector, the remaining particles on the partially filled vector,

| Color gradient angle $\theta_G$ | Ordered list of lattice vectors |
|---|---|
| $\theta_G \in (0, \frac{\pi}{8})$ | $e_1, e_5, e_8, e_2, e_0, e_4, e_6, e_7, e_3$ |
| $\theta_G \in (\frac{\pi}{8}, \frac{\pi}{4})$ | $e_5, e_1, e_2, e_8, e_0, e_6, e_4, e_3, e_7$ |
| $\theta_G \in (\frac{\pi}{4}, \frac{3\pi}{8})$ | $e_5, e_2, e_1, e_6, e_0, e_8, e_3, e_4, e_7$ |
| $\theta_G \in (\frac{3\pi}{8}, \frac{\pi}{2})$ | $e_2, e_5, e_6, e_1, e_0, e_3, e_8, e_7, e_4$ |
| $\theta_G \in (\frac{\pi}{2}, \frac{5\pi}{8})$ | $e_2, e_6, e_5, e_3, e_0, e_1, e_7, e_8, e_4$ |
| $\theta_G \in (\frac{5\pi}{8}, \frac{3\pi}{4})$ | $e_6, e_2, e_3, e_5, e_0, e_7, e_1, e_4, e_8$ |
| $\theta_G \in (\frac{3\pi}{4}, \frac{7\pi}{8})$ | $e_6, e_3, e_2, e_7, e_0, e_5, e_4, e_1, e_8$ |
| $\theta_G \in (\frac{7\pi}{8}, \pi)$ | $e_3, e_6, e_7, e_2, e_0, e_4, e_5, e_8, e_1$ |
| $\theta_G \in (\pi, \frac{9\pi}{8})$ | $e_3, e_7, e_6, e_4, e_0, e_2, e_8, e_5, e_1$ |
| $\theta_G \in (\frac{9\pi}{8}, \frac{5\pi}{4})$ | $e_7, e_3, e_4, e_6, e_0, e_8, e_2, e_1, e_5$ |
| $\theta_G \in (\frac{5\pi}{4}, \frac{11\pi}{8})$ | $e_7, e_4, e_3, e_8, e_0, e_6, e_1, e_2, e_5$ |
| $\theta_G \in (\frac{11\pi}{8}, \frac{3\pi}{2})$ | $e_4, e_7, e_8, e_3, e_0, e_1, e_6, e_5, e_2$ |
| $\theta_G \in (\frac{3\pi}{2}, \frac{13\pi}{8})$ | $e_4, e_8, e_7, e_1, e_0, e_3, e_5, e_6, e_2$ |
| $\theta_G \in (\frac{13\pi}{8}, \frac{5\pi}{2})$ | $e_8, e_4, e_1, e_7, e_0, e_5, e_3, e_2, e_6$ |
| $\theta_G \in (\frac{5\pi}{2}, \frac{15\pi}{8})$ | $e_8, e_1, e_4, e_5, e_0, e_7, e_2, e_3, e_6$ |
| $\theta_G \in (\frac{15\pi}{8}, 2\pi)$ | $e_1, e_8, e_5, e_4, e_0, e_2, e_7, e_6, e_3$ |

Table 3.1: Ranked list of the lattice vectors versus angle of the color gradient $\theta_G$ from nearest to furthest on the D2Q9 lattice. A schematic diagram of the velocity vectors $e_i$ can be found in figure 2.2.

and all particles on any remaining vectors, are declared "blue". At the end of this process, all vectors except one will be purely red or blue.

The method provides a very sharp interface, since only one vector has a mixture of red and blue particles. On the other hand this method does not give a continuous dependency between the color gradient angle and the resultant color flux. If the color gradient is perturbed so that it crosses one of the thresholds in table 3.1, the resultant color flux is discontinuously altered.

Latva-Kokko and Rothman [57] found that this primitive recoloring also suffered from an anomaly called lattice pinning. If an interface is close to a node it can be immobilised even if there is a field-scale flow velocity for the fluid at-large. The problem was seen to be highly prevalent in the case of small red droplets immersed in blue fluid, where it was observed that droplets with a radius less than 1.13 are always pinned, while droplets with a radius less than 1.59 ran a risk of being pinned.

D'Ortona *et al.*[58] introduced a formula-based recoloring scheme. This improved the isotropy and reduced the lattice pinning problem at the cost of making the interface more diffuse. In this method, the new distributions are given by

$$f_i'^R = f_i^R + \beta \phi^R \phi^B \cos(\varphi_i) \tag{3.11}$$
$$f_i'^B = f_i^B - \beta \phi^R \phi^B \cos(\varphi_i), \qquad i = 1, \ldots, 8 \tag{3.12}$$

where $\phi^a$ is the particle fraction of component $a$, $\varphi_i$ is the angle between the lattice vector $\boldsymbol{e}_i$ and the color gradient, and $\beta$ is a parameter regulating the degree of phase separation, and is usually set between 0 and 1. If $\beta > 1$ the realizability constraint may be violated, while $\beta = 0$ yields no phase separation. Increasing $\beta$ creates sharper interfaces, but the problem of lattice-pinning can crop up, droplets of radius below 0.75 lattice units may be completely pinned, while droplets of radius below 1.8 lattice units may suffer lesser pinning effects. Decreasing $\beta$ to 0.8 removes the possibility of total pinning almost entirely, although there are still moderate effects for droplets with radius below 1.8 lattice units [57].

After the recoloring, the collision step is complete, and the next time step commences with the propagation step (3.2).

Gunstensen and Rothman [12] employed the color model for porous media flow simulations in 1993, with perfect wetting ($|\cos\theta| > 1$ in equation 1.14), and determined the nature of the flow for different saturations and external forces. Wetting effects are handled by assigning a color content to wall nodes. These will then contribute to the color gradient like any other cell [58]. More specifically, each wall node is assigned a value $\Theta(\boldsymbol{x})$. The fictitious red color content of a wall node $\boldsymbol{x}$ is then

$$\rho^R = \Theta(\boldsymbol{x})\rho, \tag{3.13}$$

where $\rho$ is the average density of the surrounding fluid. The fictitious blue color content of a wall node is 0. Although the $\rho^R$ and $\rho^B$ of a wall node can be radically different from the densities in nearby fluid nodes, for example if $\Theta < 0$ the fictional density of red particles is negative. However, it is the density difference $\rho^R - \rho^B$, and not $\rho^R$ and $\rho^B$ themselves, which enters into the calculation of the color gradient, so this is not a concern. For a completely red wetting wall $\Theta \leq 1$, while $\Theta \geq 1$ indicates a completely blue wetting wall. For $-1 < \Theta < 1$, the wall is partially wetting [59], while $\Theta = 0$ indicates neutral wetting. For a perfectly sharp interface with no hysteresis arising from lattice pinning, Latva-Kokko and Rothman also showed that the predicted contact angle is given by

$$\cos\theta = \Theta. \tag{3.14}$$

The color model was important in that it opened up the opportunity to employ lattice-Boltzmann models for two-phase flow. Disadvantages of the model include a level of anisotropy in surface tension, and that the recoloring step is computationally demanding [23].

An advantage of the chromodynamic model is that the surface tension can be approximated *a priori* without experimental trials [55]. The analysis by Reis and Phillips [52] showed that

$$\sigma \sim A\tau. \tag{3.15}$$

## 3.2   Shan-Chen model

The second model to simulate two-phase flow was introduced by Shan and Chen in 1993 [60] and further analysed in 1994 [61]. It is referred to as the Shan-Chen model or the "pseudo-potential" model.

The model can simulate multiphase flows with one component (such as water and vapor) or multiple components (such as water and oil). The idea in the Shan-Chen model is to implement a direct repulsive force between particles in each phase, and applying this to the equilibrium velocity. In general, the forces are limited to the nearest neighbors. With a hexagonal lattice, this means each node is affected by each of its six neighbors. For the square lattice the nodes $\sqrt{2}$ away are also included. It is possible to extend the model to implement forces between nodes further away as well, this is common when using MRT collision operators. (See for example Sbragaglia *et al.* [62].)

In the single component case, a function $\psi(\rho(\boldsymbol{x})) = \psi(\boldsymbol{x})$ is calculated at each node, and the new equilibrium velocity $\boldsymbol{u}'$ is then given by

$$\boldsymbol{u}' = \boldsymbol{u} - \psi(\boldsymbol{x}) \sum_{\boldsymbol{x}'} \mathscr{G}(\boldsymbol{x}, \boldsymbol{x}')\psi(\boldsymbol{x} + \boldsymbol{x}')(\boldsymbol{x}' - \boldsymbol{x}). \tag{3.16}$$

Here, $\mathscr{G}$ is a Green's function [60]; the definition of a Green's function can be found in textbooks such as Evans 2.2.4 [63]. Usually, only forces between neighboring cells are accounted for. In the case of the square D2Q9 lattice, this includes cells sharing a corner. Note that applying the forces by substituting $\boldsymbol{u}$ with $\boldsymbol{u}'$ is the same method used to implement external forces. For the D2Q9 case, $\mathscr{G}$ can be written as

$$\mathscr{G} = \begin{cases} G/9, & |\boldsymbol{x} - \boldsymbol{x}'| = c \\ G/36, & |\boldsymbol{x} - \boldsymbol{x}'| = c\sqrt{2} \\ 0, & |\boldsymbol{x} - \boldsymbol{x}'| > c\sqrt{2}. \end{cases} \tag{3.17}$$

With $\mathscr{G}$ defined, (3.16) becomes

$$\boldsymbol{u}' = \boldsymbol{u} - \psi(\boldsymbol{x})G \sum_{a=1}^{8} \psi(\boldsymbol{x} + \boldsymbol{e}_i)\boldsymbol{e}_i. \tag{3.18}$$

The name "pseudo-potential" comes from defining an interaction potential $\Psi$

$$\Psi(\boldsymbol{x}, \boldsymbol{x}') = \mathscr{G}\psi(\boldsymbol{x})\psi(\boldsymbol{x}'), \tag{3.19}$$

when (3.18) can be written as $\boldsymbol{u}' = \boldsymbol{u} - \nabla\Psi$ when $c \to 0$.

For the SCMP models, several functions for $\psi$ have been proposed, each leading to different equations of state [64]. Shan and Chen 1994 used

$$\psi(\rho) = \psi_0 \exp(-\frac{-\rho_0}{\rho}). \tag{3.20}$$

Note that the simple $\psi = \rho$ does not work and will lead to mass collapse, where the density can increase indefinitely for certain nodes [65]. The actual $\psi(\rho)$ used (3.20) approaches a constant for large $\rho$, effectively limiting the maximum density.

The pressure tensor for the fluid is given by [61, 66]

$$\boldsymbol{P} = \sum_i f_i \boldsymbol{e}_i \boldsymbol{e}_i + \frac{G}{2}\psi(\boldsymbol{x}) \sum_i w_i \psi(\boldsymbol{x} + \boldsymbol{e}_i) \boldsymbol{e}_i \boldsymbol{e}_i, \tag{3.21}$$

where the first term accounts for the ideal pressure, while the second accounts for the separation forces.

In the multicomponent case, each component can be tagged "red" or "blue" as with the color model. A separation force is implemented between particles of opposite colors. Particles of the same color usually have no special forces between them.

For each node, the functions $\psi^R$ and $\psi^B$ need to be calculated for each phase. Unlike the the single-component case, the multicomponent model does not risk mass collapse since forces are only present at the interface, so $\psi^a$ can simply be defined as

$$\psi^a(\boldsymbol{x}) = \rho^a(\boldsymbol{x}). \tag{3.22}$$

The pseudo-potential between two nodes $\boldsymbol{x}_1$ and $\boldsymbol{x}_2$ is denoted $\Psi^{a\hat{a}}(\boldsymbol{x}_1, \boldsymbol{x}_2)$ and given by

$$\Psi^{a\hat{a}}(\boldsymbol{x}_1, \boldsymbol{x}_2) = \psi^a(\boldsymbol{x}_1)\mathscr{G}^{a\hat{a}}(\boldsymbol{x}_1, \boldsymbol{x}_2)\psi^{\hat{a}}(\boldsymbol{x}_2). \tag{3.23}$$

As in the single-component model, $\mathscr{G}^{a\hat{a}}$ is a Green's function, and serves as a separation parameter regulating the interface strength. For the D2Q9 lattice, $\mathscr{G}^{a\hat{a}}$ is given by (see for example [48])

$$\mathscr{G}^{a\hat{a}} = \begin{cases} G^{a\hat{a}}/9 & \text{if } |\boldsymbol{x}_1 - \boldsymbol{x}_2| = c \\ G^{a\hat{a}}/36 & \text{if } |\boldsymbol{x}_1 - \boldsymbol{x}_2| = \sqrt{2}c \\ 0 & \text{otherwise,} \end{cases} \tag{3.24}$$

where $G^{a\hat{a}}$ is now a scalar parameter controlling the repulsion or attraction between components $a$ and $\hat{a}$, and $w_i$ are the same weights for $e_i$ characteristic of the D2Q9 problem.

The momentum change caused by this pseudo-potential on phase $a$ is given by

$$\frac{d(\rho u)}{dt} = -\psi^a(x)G^{a\hat{a}} \sum_i \psi^{\hat{a}}(x+e_i)e_i. \qquad (3.25)$$

The new $u$ is used when calculating $f^{a(eq)}$.

If the separation parameter $G^{a\hat{a}}$ is larger than the critical coupling constant $G_C$, the separation forces will overcome the diffusive effects and phase segregation is possible. A slightly perturbed mixture of fluids will spontaneously separate, with one of the phases forming circular droplets within the other phase [60]. If $G^{a\hat{a}} < G_C$, the phases will not separate and a uniform mixture of red and blue particles will be the eventual result.

The exact value of $G_C$ is often difficult to determine analytically, although Martys and Douglas [67] gave an expression for phases with equal viscosity and particle mass. In general, $G_C$ is smallest if the number of particles for each component is equal. If the average fraction of one component approaches zero, $G_C$ approaches infinity. Illustration of this phase separation is shown in chapter 4.
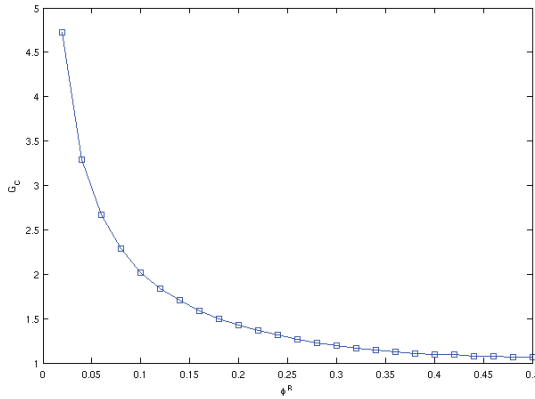


Figure 3.1: Critical coupling constant $G_C$ versus average fraction of red particles in a binary mixture, with $\tau^R = \tau^B = 1$.

Even with $G > G_C$, the phases are not entirely pure. Smaller values of $G^{a\hat{a}}$ yield more diffuse interfaces and higher levels of impurity in each phase. On the

other hand, the interfaces feature spuriously large macroscopic currents due to the repulsive forces, and limiting these suggests that a lower $G$ is better [48].

The original paper by Shan and Chen showed that the density difference between the interior and exterior of the droplets are proportional to the inverse of the droplets' radii. If the ideal gas equation is used, the density difference is proportional to the pressure difference, which means that the density difference was in accordance with Laplace's law.

$$\rho^R - \rho^B = \frac{\lambda}{R},$$
(3.26)

where $\lambda$ is the surface tension coefficient. However, the strong interparticle forces in the Shan-Chen model mean that the fluids are not ideal, and the pressure to density ratio are larger in mixed fluid regions. In chapter 4 we see that this matters for small droplets where even the center of the droplet is a mixed fluid region. Nonetheless, assuming moderate $G$, Laplace's law is adhered to if the nonideal pressure terms are accounted for. For very large values of $G$, the magnitude of the spurious currents are too large to maintain observation of Laplace's law.

Implementation of wetting was explored by Martys and Chen [24] by implementing a force similar to equation (3.16). If $s(\boldsymbol{x})$ is the wall matrix ($s = 0$ for a fluid node, $s = 1$ for a solid node), the interaction force between the wall and fluid component $a$ is given by

$$\boldsymbol{F}^{aw}(\boldsymbol{x}) = -\psi^a(\boldsymbol{x}) \sum_i \mathscr{G}^{aw} s(\boldsymbol{x} + \boldsymbol{e}_i) \boldsymbol{e}_i,$$
(3.27)

where, like in equation (3.24), $\mathscr{G}^{aw}$ is dependent on the vector along which the force acts:

$$\mathscr{G}^{aw} = \begin{cases} G^{aw}/9 & \text{if } |\boldsymbol{x}_1 - \boldsymbol{x}_2| = c \\ G^{aw}/36 & \text{if } |\boldsymbol{x}_1 - \boldsymbol{x}_2| = \sqrt{2}c \\ 0 & \text{otherwise} \end{cases}$$
(3.28)

The scalar parameters $G^{aw}$ for different phases $a$ can be tuned to determine the identity of the wetting phase and the strength of the wetting. Martys and Chen note that phase $a$ is wetting while $\hat{a}$ is non-wetting if $G^{aw}$ is negative and $G^{\hat{a}w}$ is positive [24]. A more general condition for $a$ to be wetting with respect to $\hat{a}$ is that $G^{aw} < G^{\hat{a}w}$. Note that this implementation means that wetting is controlled by two wetting parameters, $G^{Rw}$ and $G^{Bw}$, instead of a single wetting parameter $\Theta$ as in the color model.

Sukop and Thorne's textbook [48] (p. 114) estimate the contact angle by a straightforward substitution $\sigma \to G$ in Young's equation 1.14 to obtain

$$\cos\theta = \frac{G^{aw} - G^{\hat{a}w}}{G^{a\hat{a}}}$$
(3.29)

In equation 3.29, $a$ is the phase of the droplet adhering to the wall while $\hat{a}$ is the other phase.

The contact angles were also studied by Benzi *et al.* [68], Kang *et al.* [69] and Huang *et al.* [70] The latter proposed that the contact angle can be approximated with

$$\cos\theta = \frac{G^{aw} - G^{\hat{a}w}}{G^{a\hat{a}} \frac{\rho^a - \rho^{\hat{a}}}{2}},\tag{3.30}$$

and conducted numerical experiments to verify this as an improvement over equation (3.29). While Huang *et al.* call equation (3.30) "similar" to (3.29), the resulting contact angle appears to be radically different unless $\rho^a - \rho^{\hat{a}} \approx 2$. Equation (3.30) is used in Chapter 4 of this thesis. The density of fluid $a$ in the droplet is denoted $\rho^a$, while $\rho^{\hat{a}}$ is the density of $\hat{a}$-particles in phase $a$ (that is, the density of the stray particles of the continuous component within the disperse phase). Comparisons of the Shan-Chen method with laboratory experiments were conducted by Schaap *et al.* [71]

Due to the Shan-Chen method's relative simplicity, and ease of implementation, it is the among the most popular methods used in practice for two-phase lattice-Boltzmann simulations [23]. Sukop and Thorne [48] present this method as the introductory method for multicomponent multiphase flow.

## 3.3   Other multiphase Lattice-Boltzmann methods

The color model and Shan-Chen model are only two of the numerous schemes for simulating multiphase flow with the Lattice-Boltzmann method. We have not fully studied these methods but present a brief overview here.

### 3.3.1   Free energy model

The free energy model was introduced by Orlandini *et al.* [72] and Swift *et al.* [73, 74]. These methods aim for thermodynamic consistency [23]. These methods are based on the van der Waals formulation for free energy and its associated nonideal pressure. This free energy is imposed onto the model for calculation of equilibrium distributions, and has been referred to as a "top-down" model, in contrast to the Shan-Chen model which is a "bottom-up" model [75].

Unlike the color model and Shan-Chen model which have distribution functions for red and blue particles, implementations of the free energy model usually employ distributions that represent the total of, and difference between, red and blue particles.

An advantage of the free energy method is that it accounts for equilibrium thermodynamics so that temperature can be modelled. The main drawback is a lack

of Galilean invariance [76]. The free energy model is a popular method, and has been used for porous media flow simulation, including oil recovery problems (for example Langaas [13]). A tutorial on the method has been published by Yeomans [77].

### 3.3.2 Enskog equation based methods

The Enskog based methods (also called "finite density" methods [23]) were developed by Luo in 1998 [78] as a means of achieving thermodynamic consistency. While the Boltzmann equation's validity is limited to rarefied gases, the Enskog equation [36] accounts for the particle radius. These methods are designed by discretizing the Enskog equation.

The original model by Luo was made for single component multiphase flow, but articles by Luo and Girimaji [79, 80] and Guo and Zhao [81] have extended the model to multicomponent flow. Guo and Zhao further extended the model to handle flows with different viscosities [82].

Luo noted that the model can only be first-order accurate at best [78], while Latva-Kokko and Rothmann observed that the surface tension with this model cannot be predicted *a priori* [57].

### 3.3.3 Front-tracking methods

The Langrangian front-tracking (FT) methods are a different concept from the above methods which are front-capturing. The FT models introduce a series of markers in the domain which move with the flow, and the lines connecting these markers draw out the interface. Markers may be deleted if the distance between them declines below a set threshold, or introduced if the distance between two neighboring markers move far apart [83].

Inherent advantages with the FT models are sharp rather than diffuse interfaces [23], and computational efficiency since calculations for separation effects are limited to the near-interface region rather than the entire domain [83]. The drawbacks of the FT methods are singularities and poor conditioning when the interface becomes tortuous or undergoes major qualitative changes [83].

## 3.4 Solute flow

When one species (the solute) is dissolved in another (solvent), there are multiple particles in the domain which need to be taken into account. Solute flow is different from two-phase flow since there generally are no phase separation forces, and the number of solvent particles far exceeds the number of solute particles.

In lattice Boltzmann models, solute flow has been used e.g. to track the flow of dissolved acid in order to monitor the corrosive effects this has on the wall [84].

In a fluid with a solute species, the relative rarity of the solute particles means that their contribution to the overall flow of the fluid can frequently be ignored. The earliest study of such systems using lattice Boltzmann were made by Dawson *et. al.* [85].

A distribution function $g$ is assigned to track the distribution of solute species, similar to the distribution function $f$ assigned to the solvent. The evolution function for $g$ is given by

$$g_i(\mathbf{x} + \mathbf{e}_i \delta t, t + \delta_t) = g_i(\mathbf{x}, t) - \frac{g_i(\mathbf{x}, t) - g_i^{(eq)}(C, \mathbf{u}, T)}{\tau_s} \qquad (3.31)$$

which is similar to the evolution function to $f$. Here, $\tau_s$ is the relaxation time which is related to the diffusivity by the relation

$$D = (\tau_s - \frac{1}{2})RT. \qquad (3.32)$$

The solute is essentially a passive component, and its flow depends on the movement of the surrounding solute. Hence, the $\mathbf{u}$ used to calculate $g^{eq}$ is calculated from $f$, not $g$.

## 3.5 Simulation of surface-tension affecting components

In our project we have aimed to model the effect surfactants have on the surface tension, and the consequences which this brings about on the fluid flow. In this section we will cover some of the existing methods and discuss the method used in this project.

Lattice Boltzmann models with surface active species are generally made to simulate the effects of emulsifiers.

### 3.5.1 Existing lattice Boltzmann models for surfactants

Lattice Boltzmann models for surfactant flow have been proposed both for the free energy model, and for the Shan-Chen model.

The first such models were designed as an extension of the free energy method. These include the binary models by Gonnella *et al.* [86] and Theissen *et al.* [87], and the ternary models by Lamura *et al.* [88, 89]

Modelling amphiphile species for Shan-Chen methods was proposed by Chen *et al.* in 2000 [90]. This model was further developed by Nekovee et al. [91] and further computational analysis and evaluation of the model was performed by Love et al. [92]. In these models, surfactants are modelled as a species with a dipolar vector indicating its orientation as well as position.

### 3.5.2 Solute flow modelling of surfactants

Our models for surfactant simulation have assumed that changes in surface tension due to the presence of a surfactant are largely proportional to the concentration of surfactant.

$$\sigma(\boldsymbol{x}) = \sigma_0 - \upsilon C(\boldsymbol{x}). \tag{3.33}$$

Equation (1.21) gives some justification for this assumption, and earlier works by Greenspan [18, 19], who studied surface tension effects in cell biology research, made this assumption in the mathematical analysis.

There is a lower bound for $\sigma(\boldsymbol{x})$, requiring the parameter to be non-negative. The presence of the critical micelle concentration, above which additional surfactant will form non-active micelles, suggests that setting the lower bound higher may be justified as well.

Both the color model and the Shan-Chen model have been employed. In both cases, the surfactant component was modelled as a solute component as described in Section 3.4. The concentration $C$ of the solute is defined as

$$C(\boldsymbol{x}) = \sum_i g_i(\boldsymbol{x}), \tag{3.34}$$

where $g$ is the distribution function for the solute.

**Color model**

In the color model, the magnitude of surface tension is controlled through the parameter $A$ (3.8). Conveniently, the surface tension is proportional to this parameter, and since the process at an arbitrary site $\boldsymbol{x}$ happens independently of all other sites, reducing the surface tension is easily effected by reducing the parameter $A$ by a figure proportional to the concentration.

$$A(\boldsymbol{x}) = A_0 - \eta C(\boldsymbol{x}), \tag{3.35}$$

where $A_0$ is the default surface tension parameter in the absence of any surfactant.

**Shan-Chen model**

A number of properties in the Shan-Chen model model make it more difficult to
simulate the effect of a surfactant species. The surface tension is caused by the
force in equation (3.16), and the parameter which regulates the surface tension is
$G$. However, the process at site $x$ is dependent on sites $x + e_i$ as well, so imple-
menting a spatial variation in $G$ violates the symmetry required for conservation
of momentum. This problem can be worked around by instead reducing the po-
tential $\psi(x)$ by a factor $d(x)$, which maintains the symmetry.

The surface tension coefficient $\sigma$'s dependency on $G$ is not completely known,
even though $\sigma$ generally increases with $G$ and Chin *et al.* [75] found the relation-
ship to be approximately linear.

At $\tau = 1$, we found $\sigma$ to be approximately proportional to $G - 1$, and defined
the reduction factor

$$d(x) = \max(0, \sqrt{1 - \zeta C(x)/2}). \tag{3.36}$$

This method allowed us to reduce the surface tension in the Shan-Chen model
as well. An additional difficulty is that equation (3.16) regulates the phase sepa-
ration as well as the surface tension, so an area with reduced surface tension will
also have a more diffuse interface.

### 3.5.3   Comparison of the models

If we compare the method used in this thesis to the one presented by Chen *et al.*
[90], we can find the following differences.

Chen *et al.* takes into account the dipolar nature of the amphiphile species.
This is necessary since the amphiphile species in Chen *et al.* actively exerts forces
on the other, non-amphiphile, species, and the force exerted is dependent on the
orientation of the amphiphile particles. In our model, the surfactant does not
exert any forces directly, rather it causes a change in $\psi$, and this affects the non-
amphiphile species forces upon each other. Our model cannot simulate unaligned
amphiphile species, where the dipolar amphiphile particles are not pointing in the
same direction, weakening their overall effect, however we can simulate the entire
removal of phase separation allowing perfect mixture if this is desired.

In Chen *et al.*, the forces on the amphiphile species cause them to naturally
adsorb to the oil-water interface. In our model we implemented a separate "force"
on the surfactant solute in order to emulate a similar effect. The force we im-
plemented on the solute does not cause any movement in the solvent fluids, our
assumption that the mass of is much smaller than the mass of solvent is the reason
we can set aside the constraint of Newton's third law for solute-solvent interac-
tions.

Our model is less computationally demanding the Chen *et al.* model, because we do not need to calculate the complex force terms between amphiphile species and non-amphiphile species ($F^{s,c}$ and $F^{c,s}$) or the inter-amphiphile species forces $F^{s,s}$.

# Chapter 4

# Basic simulation samples

In this chapter we demonstrate some of the properties the different two-phase Lattice Boltzmann models possess. We have examined the color model and Shan-Chen model.

In Section 4.1 we deal with a pure phase separation scenario, where there are no walls. In Section 4.2 the effect of non-wetting walls are examined. The effect wetting has on the separation process and final state is covered in Section 4.3.

## 4.1   Phase separation

If two immiscible fluid components are mixed together, they will separate into phases due to the immiscibility. All the major methods for multiphase Lattice Boltzmann methods are able to simulate this separation, although some of the methods have parameters that need to be large enough to effect this.

Assuming a domain with no walls or external forces, there will be no phase separation if the mixture is exactly homogeneous. Such a mixture is an example of an unstable equilibrium, where the lack of any concentration gradient and exact cancellation of all forces results in no net movement of either component. Random fluctuations and perturbations make such a delicate situation impossible for real fluids, but for a Lattice-Boltzmann simulation, a perturbation from homogeneity is needed if the fluids are to separate.

To illustrate phase separation, we started with a mixture of two immiscible fluids, generically labelled "red" and "blue". The fluid properties of the mixture are identical, with relaxation time $\tau = 1$. The initial state is a uniform mixture of 30% red particles and 70% blue particles, with a small $\pm 1\%$ concentration perturbation at each grid cell.
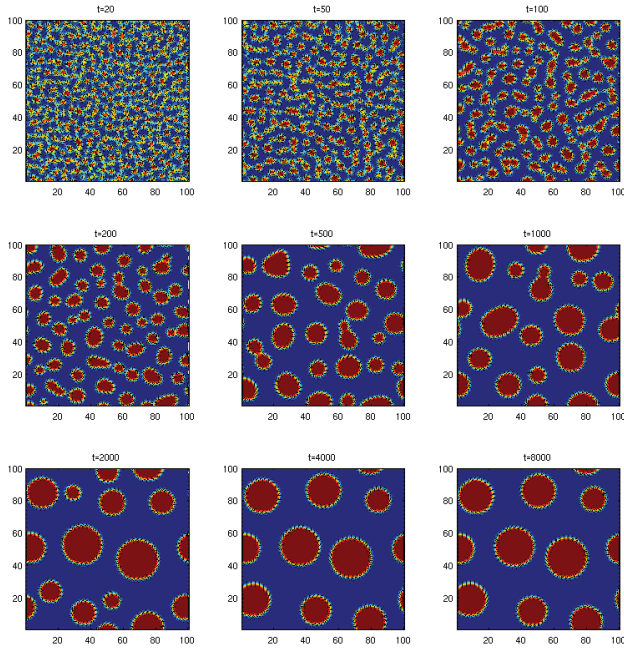
## 4.1.1  Separation in the color model



Figure 4.1: Phase separation in the color model from an initially near uniform mixture of immiscible red and blue particles ($\phi^R = 0.3 \pm 0.01$). Surface tension parameter $A = 0.15$.

Our example of the separation which takes place in the color model is shown in Figure 4.1. In this model, we operated with a surface tension coefficient of $A = 0.15$.

The formation very small droplets with a radius of order 1–2 grid cells is already visible after 20 time steps, and by $t = 100$, the mixed fluid region is confined to the interface only. Over the next time steps, we observe the coalescence of the small droplets to form larger droplets, but this process slows down as the mean distance between individual droplets increases. Indeed, the process appears to have stalled between $t = 4000$ and $t = 8000$.
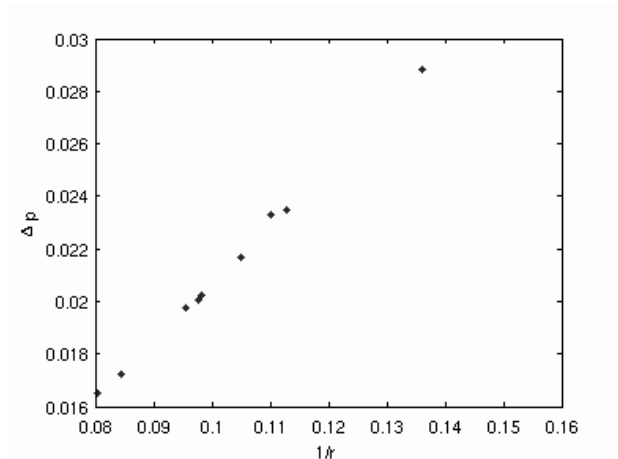
Figure 4.2: Pressure difference between droplet interior and exterior versus the inverse of the droplet radius for each of the nine droplets in figure 4.1 for $t = 8000$.

The droplets assume a circular shape since this minimises the surface energy. The occasional oblong droplet is due to the coalescence of two smaller droplets, but these eventually assume a circular shape. Note that the model does not have a barrier or membrane between individual droplets, so flocculation without coalescence is not observed.

Analysing the interior pressure of each of the nine droplets and comparing this to the droplets' radii, as shown in Figure 4.2 shows that Laplace's law (1.11) is adhered to.

### 4.1.2   Separation in the Shan-Chen model

An example of the separation process in the Shan-Chen model is shown in Figure 4.3. For this model, we used set separation parameter $G = 1.6$. For separation to take place at all, it is required that $G > G_c$, where $G_C$ is the critical separation parameter. For $G < G_C$, the diffusion will be greater than the separation, and the red and blue fluids will be effectively miscible, leading asymptotically to a uniform distribution of red and blue particles.

Even with $G > G_C$, the phases are not entirely pure, each of the phases has stray particles which belong in the other phase. For the $G = 1.6$ example, about 5% of the particles are stray. The presence of stray particles is a result of the highly diffuse interface. Raising $G$ increases the separation forces and reduces the number of stray particles, but the stronger separation forces also damage the
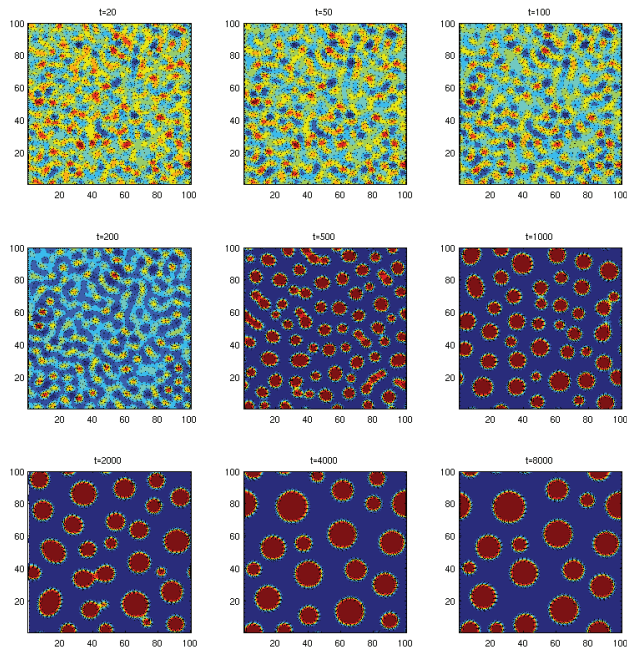
Figure 4.3: Phase separation in the Shan-Chen model from an initially near uniform mixture of immiscible red and blue particles ($\phi^R = 0.3 \pm 0.01$), separation parameter $G = 1.6$.
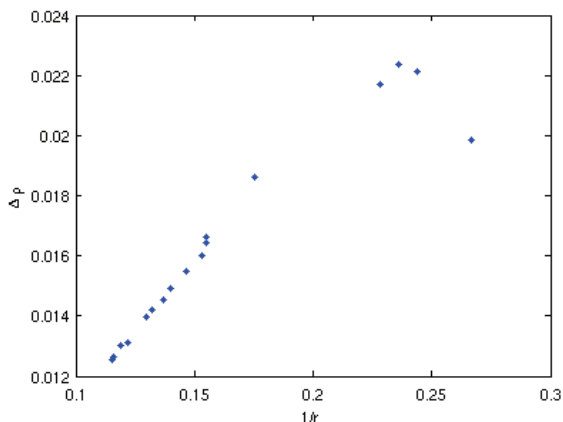
Figure 4.4: Density difference between droplet interior and exterior versus the inverse of the droplet radius for each of the seventeen droplets in figure 4.4 for $t = 8000$.

isotropy.

The separation forces translate to a non-ideal pressure term when both red and blue particles are present. For the larger droplets, the non-ideal terms are not large, and comparing the density difference between the droplets' interiors and exterior to the radius of the droplet will yield Laplace's law. For very small droplets, the presence of stray blue particles, even at the droplet center, causes a significant reduction in density, and this is shown as the outlier to the right on Figure 4.4. Laplace's law is observed even for the smallest droplets if the nonideal pressure terms are accounted for.

## 4.2   Nonwetting walls

In the previous section, we saw that the red particles were the disperse phase, while the blue particles made up the continuous phase. This was because the red particles were in the minority. The blue particles in the majority drive the red particles together into droplets. The introduction of walls to the domain adds another element to the separation process. A particle in a fluid node next to a wall will only not experience any separation forces in the directions from the wall nodes. The result is that if the minority component is driven towards the wall, it is likely to stay there, and so the sites near the wall have a disproportionately large

percentage of the minority particle. The nodes near corners are particularly likely to be occupied by the minority component. Figures 4.5 and 4.6 illustrate this.
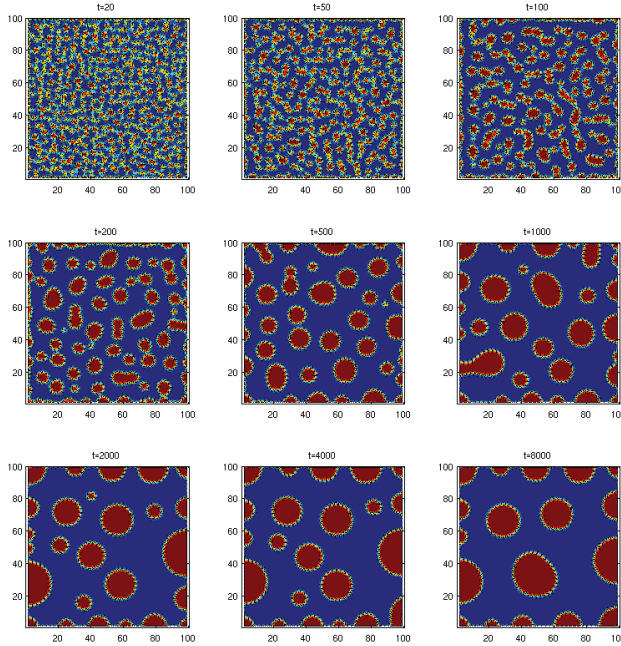


Figure 4.5: Phase separation in the color model from an initially near uniform mixture of immiscible red and blue particles ($\phi^R = 0.3 \pm 0.01$). Surface tension parameter $A = 0.15$. The edges of the domain are fixed walls.

In figure 4.5, we see that all four corners of the domain, as well as the majority of nodes next to the wall are eventually occupied by the disperse red phase. The red particles which are far enough from the wall form circular droplets as before. The wall is capable of acquiring red droplets from a fair distance, at $t = 1000$ we see a red droplet being captured by the left wall.

The process is clearly illustrated in 4.6 where our choice of separation parameter has led to a slow separation process. At $t < 100$, we see the walls attracting red particles. The nodes a few units away from the wall lose their red particles to the wall, and become fairly blue. This in turn creates a "ripple" of red particles a few
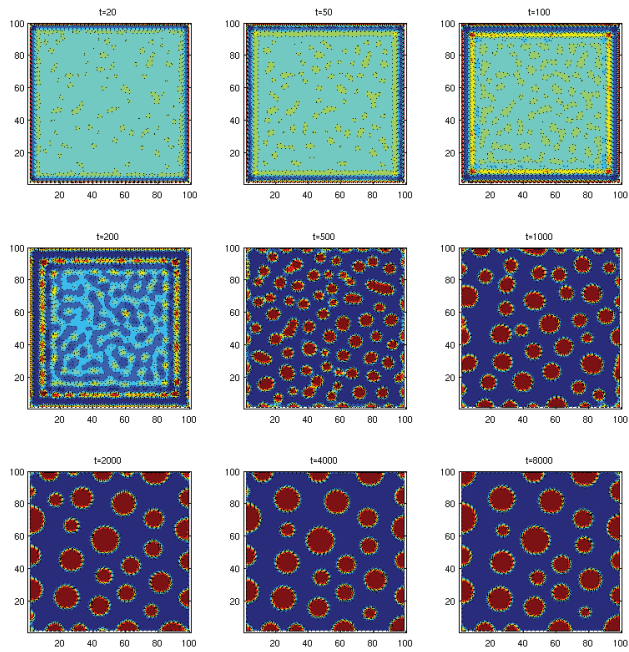
Figure 4.6: Phase separation in the Shan-Chen model from an initially near uniform mixture of immiscible red and blue particles ($\phi^R = 0.3 \pm 0.01$). Separation parameter $G = 1.6$. The edges of the domain are fixed walls.

nodes further in, as seen at $t = 100$. A weaker blue ripple is formed inside the red ripple, as seen at $t = 200$. By $t = 500$ the formation of circular droplets has settled in, and the state at $t = 8000$ is similar to that observed for the color model.

In both cases, the droplets that attach themselves to the walls have a contact angle of $\pi/2$. This is due to the walls being not being wetting with respect to any phase.

## 4.3   Wetting effects

In this section, we add the element of wetting to illustrate what effect this has on the separation process and final state.

In the case of partial wetting, both fluids may be present at the wall, and contact angles may be measured. However, direct measurement of the contact angle is challenging, because visual determination of the tangent line at the contact point is difficult. However, if we assume that a droplet on a wall is a chord of a perfect circle with radius $r$, the radius and contact angle can be found by measuring the dimensions of the droplet, a method used by both Kang *et al.* [69] and Huang *et al.* [70] for example.
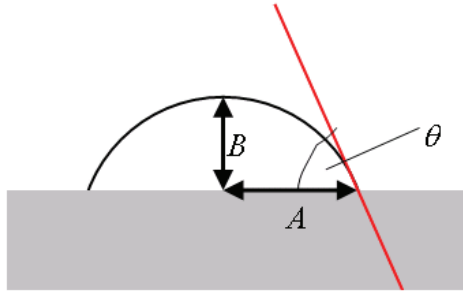


Figure 4.7: The contact angle $\theta$ can be found through equation (4.2).

Let the half the length of the contact line be $A$, and let the height of the droplet be $B$ (Figure 4.7). When measuring $A$ and $B$, we need to remember that the boundary conditions in Section 2.5.1 place the boundary halfway between the last fluid node and first wall node.

Due to Pythagoras, $A^2 + (r - B)^2 = r^2$, so the radius of the circle which the droplet is a part of is given by

$$r = \frac{A^2 + B^2}{2B}. \tag{4.1}$$

The tangent of the contact angle $\theta$ is equal to the gradient of the tangent line to the droplet at the left contact point. The gradient can be determined through (implicit) derivation of the equation of the circle evaluated at the left contact point $x = -A, y = r - B$. This gives the contact angle

$$\theta = \begin{cases} \tan^{-1}\left(\frac{2AB}{A^2-B^2}\right), & A > B \\ \frac{\pi}{2}, & A = B \\ \tan^{-1}\left(\frac{2AB}{A^2-B^2}\right) + \pi, & A < B \end{cases}. \tag{4.2}$$

In equation (4.2), the top line indicates a wetting droplet while the bottom line is a non-wetting droplet. If $A = B$, the droplets are semi-circles with tangent lines normal to the wall, and neither phase is wetting with respect to the other.

### 4.3.1   Wetting effects in the color model

To add wetting effects to the color model, we have used the process described in Section 3.1, with a wetting parameter $\Theta$ assigning a color difference for wall nodes as done in equation (3.13). Four examples of the separation process are illustrated in Figures 4.8–4.11, representing complete and partial wetting of the red and blue phase.

Figure 4.8 confirms that a completely red wetting wall will eventually cause the red fluid to spread out over the entire wall. The accumulation of red fluid near the corners of the domain was also seen for the nonwetting walls in the previous section. Likewise, no red fluid is observed at the wall if the wall is completely blue wetting as seen in Figure 4.11.

For a partially red wetting wall with $\Theta = 0.5$, illustrated in Figure 4.9, most of the red fluid adhering to the wall has accumulated in the corner, but blue fluid is present at the wall away from the corners.

For a partially blue wetting wall with $\Theta = -0,5$, red droplets do adhere to the surface but with an obtuse contact angle. Using (4.2), the contact angles are $2.2 \pm 0.1$ radians, which is slightly more than the $\frac{2\pi}{3}$ contact angle predicted by equation (3.14), but we recall that that equation assumed a perfectly sharp interface, which we do not have here.

### 4.3.2   Wetting effects in the Shan-Chen model

For the Shan-Chen model, we also present four examples representing full and partial wetting of the red and blue phase. As seen in Section 3.2, the implementation of wetting in the Shan-Chen model is controlled by two wetting parameters $G^{Rw}$ and $G^{Bw}$, as well as the coupling parameter between the two components $G^{RB}$.
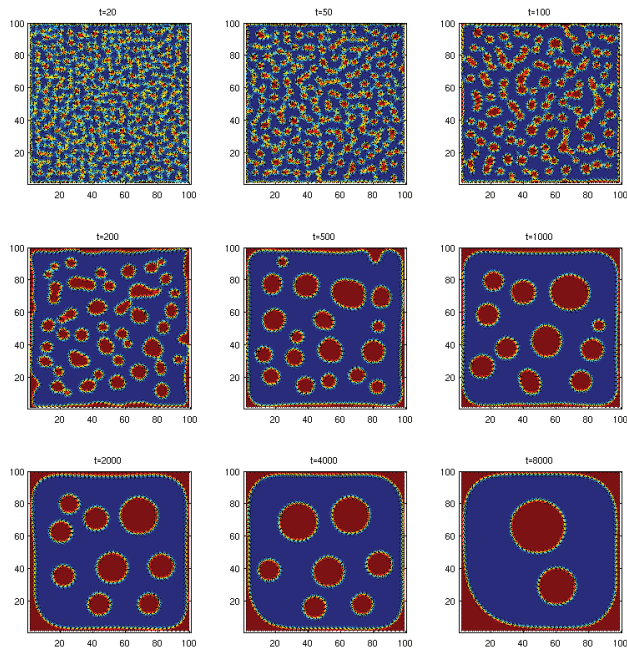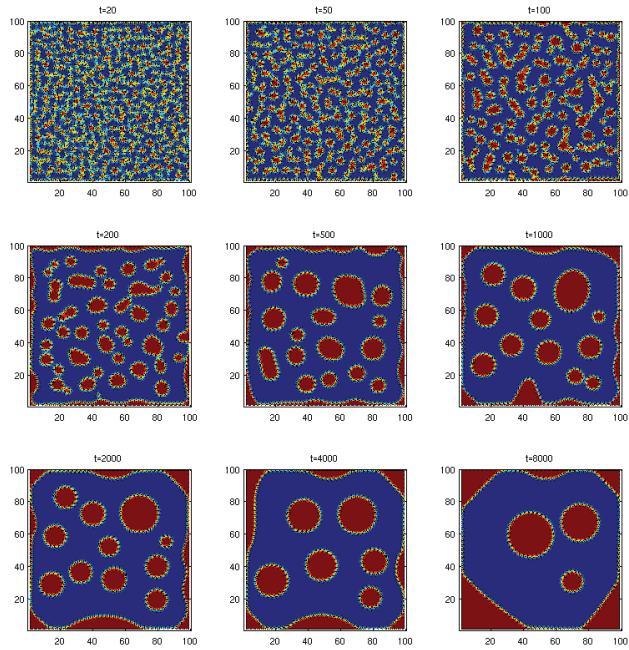
Figure 4.8: Phase separation in the color model from an initially near uniform mixture of immiscible red and blue particles ($\phi^R = 0.3 \pm 0.01$). Surface tension parameter $A = 0.15$. The edges of the domain are fixed walls which are completely red wetting ($\Theta = 1$).

Figure 4.9: Phase separation in the color model from an initially near uniform mixture of immiscible red and blue particles ($\phi^R = 0.3 \pm 0.01$). Surface tension parameter $A = 0.15$. The edges of the domain are fixed walls which are partially red wetting ($\Theta = 0.5$).
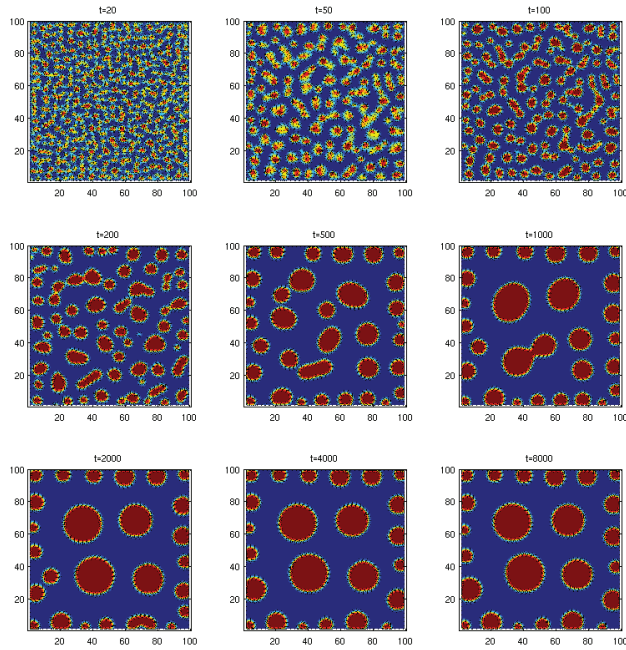
Figure 4.10: Phase separation in the color model from an initially near uniform mixture of immiscible red and blue particles ($\phi^R = 0.3 \pm 0.01$). Surface tension parameter $A = 0.15$. The edges of the domain are fixed walls which are partially blue wetting ($\Theta = -0.5$).
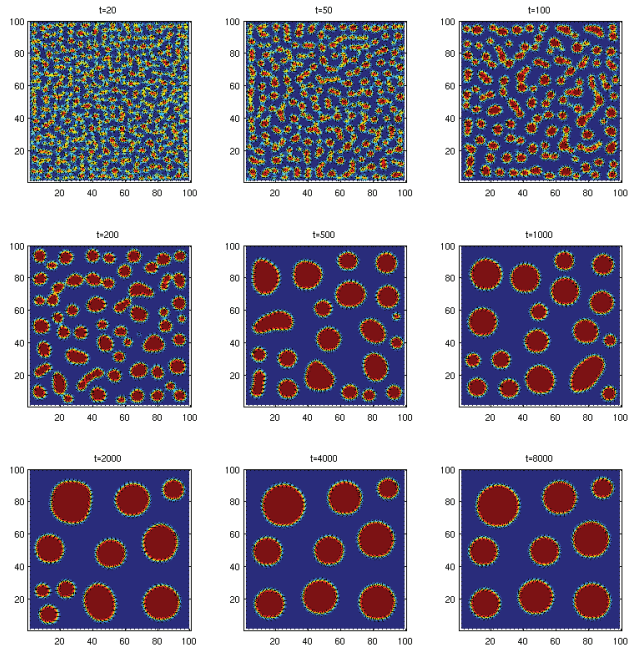
Figure 4.11: Phase separation in the color model from an initially near uniform mixture of immiscible red and blue particles ($\phi^R = 0.3 \pm 0.01$). Surface tension parameter $A = 0.15$. The edges of the domain are fixed walls which are completely blue wetting ($\Theta = -1$).

In our experiments, we have achieved the wetting by implementing an attractive force between the wetting phase and the wall, while there is no force between the nonwetting phase and the wall. For example, if red is the wetting phase $G^{Rw} < 0$ and $G^{Bw} = 0$.

According to equation (3.30), a density of $\rho = 1$, and reasonably pure phases so that the factor $\frac{\rho^a - \rho^{\hat{a}}}{2} \approx \frac{\rho^a}{2}$, total wetting requires that

$$|G^{Rw} - G^{Bw}| \geq \frac{G^{RB}}{2}, \tag{4.3}$$

which for our parameters ($\rho \approx 1, G^{RB} = 1.6$) indicates that the difference in wetting parameters must be greater than 0.8. However, we found total wetting occurred for differences in the wetting parameters slightly short of this estimate, probably due to the higher density inside the droplet. Indeed, in the examples presented here, the wetting parameter $G^{aw}$ for the wetting phase $a$, has been set to -0.75 for complete wetting. For partial wetting, $G^{aw} = -0.25$ has been used. The images of the separation process can be found in Figures 4.12–4.15.

The parameters $G^{aw} = -0.75, G^{\hat{a}w} = 0$ appear to be near the critical threshold for complete wetting when $G^{RB} = 1.6$. Reducing $G^{aw}$ slightly has left a partial wetting situation.

As seen in Section 3.2, the Shan-Chen model lacks an analytic expression to predict the contact angle, although Huang et al. found an estimate given in equation (3.30). For the partially red wetting walls (Figure 4.13), we measured the contact angles to be $1.1 \pm 0.1$ radians. For the partially blue wetting walls 4.14, the contact angles are about $1.92 \pm 0.02$ radians. With $\rho^R - \rho^B \approx 1.0$ inside the droplet, the expected contact angles are approximately 1.2 and 1.9 for the red-wetting and blue-wetting cases respectively, so our results are consistent with the estimate of Huang et al., although our measurements are not sufficiently accurate to verify the $\frac{\rho^R - \rho^B}{2}$ factor present in equation (3.30).
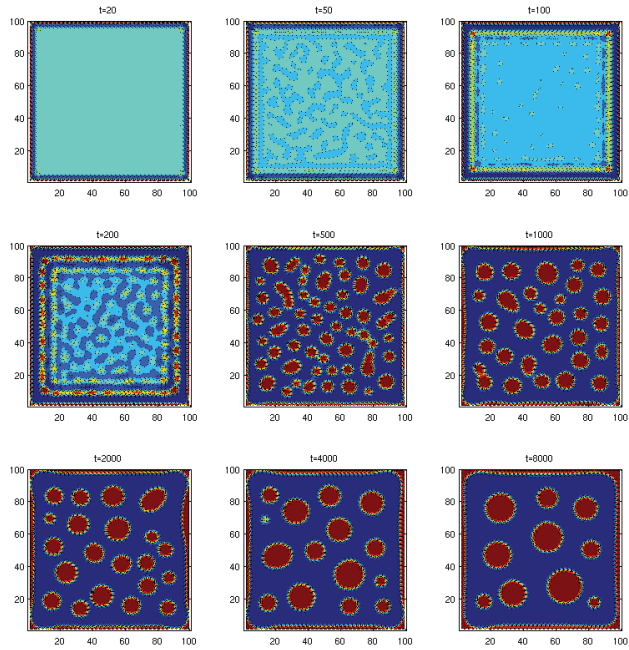
Figure 4.12: Phase separation in the Shan-Chen model from an initially near uniform mixture of immiscible red and blue particles ($\phi^R = 0.3 \pm 0.01$). Surface tension parameter $G^{RB} = 1.6$, wetting parameters $G^{Rw} = -0.75, G^{Bw} = 0$ (completely red wetting).

Figure 4.13: Phase separation in the Shan-Chen model from an initially near uniform mixture of immiscible red and blue particles ($\phi^R = 0.3 \pm 0.01$). Surface tension parameter $G^{RB} = 1.6$, wetting parameters $G^{Rw} = -0.25$, $G^{Bw} = 0$ (partially red wetting).

Figure 4.14: Phase separation in the Shan-Chen model from an initially near uniform mixture of immiscible red and blue particles ($\phi^R = 0.3 \pm 0.01$). Surface tension parameter $G^{RB} = 1.6$, wetting parameters $G^{Rw} = 0, G^{Bw} = -0.25$ (partially blue wetting).
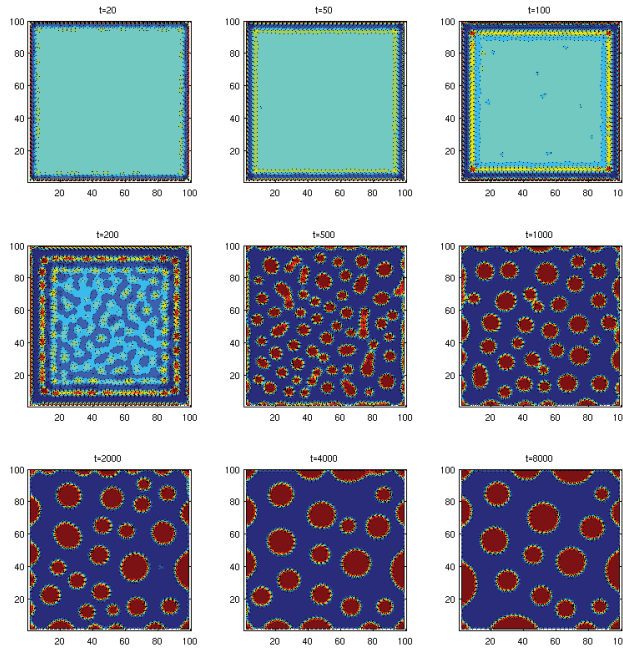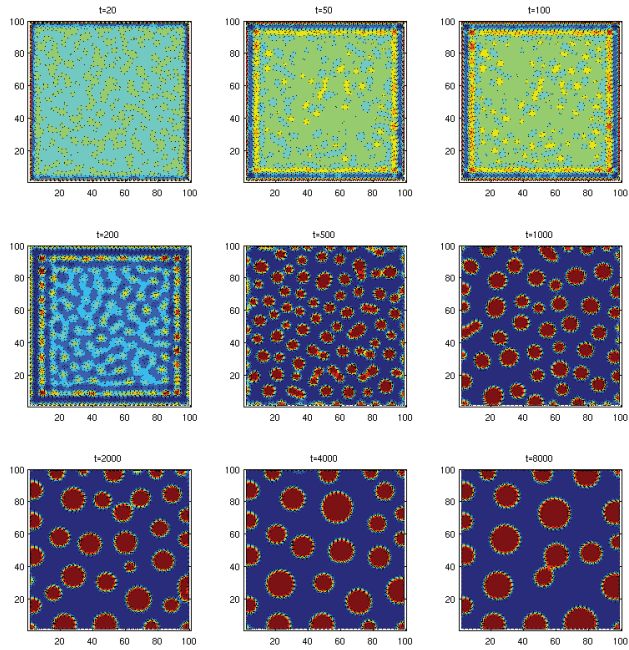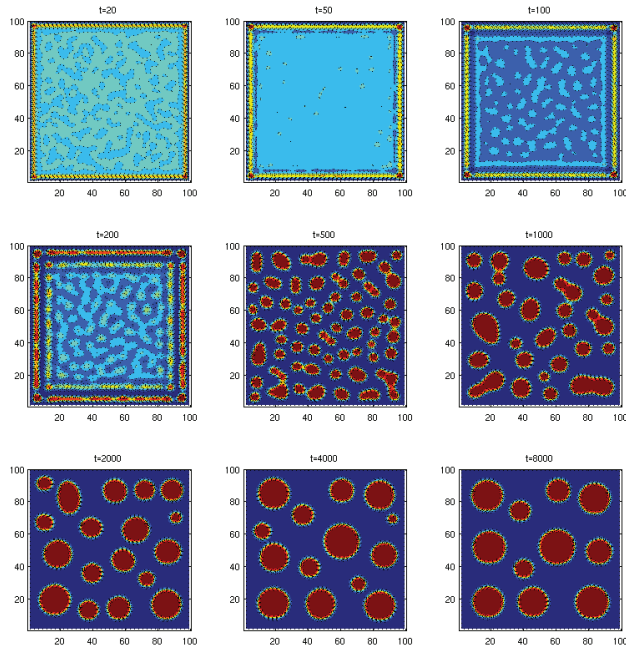
Figure 4.15: Phase separation in the Shan-Chen model from an initially near uniform mixture of immiscible red and blue particles ($\phi^R = 0.3 \pm 0.01$). Surface tension parameter $G^{RB} = 1.6$, wetting parameters $G^{Rw} = 0, G^{Bw} = -0.75$ (completely blue wetting).

# Chapter 5

# Summary

## 5.1 Papers included

The thesis includes four papers:

### 5.1.1 Paper A

Paper A, "Simulation of multiphase flows with variable surface tension using the Lattice Boltzmann method" was presented at the Fifth International Conference on Computational and Experimental Methods in Multiphase and Complex Flow, June 15–17, 2009 in New Forest, England.

The article is the first to cover the surfactant model discussed in Section 3.5.2. The physical aspects of how to lower the surface tension for the color model and Shan-Chen models are discussed.

Paper A also includes a demonstration of the lattice Boltzmann method applied to a scenario where a circular droplet is subjected to surfactant at opposite ends. The deformation this causes to the droplet is investigated. The scenario has previously been investigated experimentally by Greenspan [19], and numerically by Sapir and Nir [20], and by Li and Lubkin [21]. Our results which show a relatively small deformation are consistent with the previous numerical results.

### 5.1.2 Paper B

Paper B, "Lattice Boltzmann simulations of the motion induced by variable surface tension" was submitted to Advances in Engineering Software in September 2009 and awaiting review.

The article is an extension of paper A by investigating the numerical aspects of the model. While paper A demonstrated that the model was *qualitatively* con-

sistent with previous simulations, paper B investigates the surfactant model's numerical consistency with known analytic results. We compare our model to a result originally published by Levich and Kuznetzov [10], who found an analytic expression for the velocity of a circular droplet with a constant surface tension gradient.

Our simulations are made to verify that the lattice Boltzmann model is consistent with this analytic result, for a variety of different droplet radii, surface tension gradients, and fluid viscosities. The results showed that the color model version gave very good adherence to theory. The Shan-Chen method also gave consistent results for some parameters, but the difficulty in determining the surface tension make the results here less accurate.

### 5.1.3  Paper C

Paper C, "Simulations of the passage of droplets through narrow capillaries using the lattice Boltzmann method" was submitted to the International Journal of Numerical Analysis and Modelling in November 2009 and awaiting review.

This article uses the color model version of our model with walls and wetting effects. The purpose is to investigate a situation where a droplet in a wide space is pushed into a narrow capillary forcing it to deform. The wetting and surface tension act against this deformation, which may impede the droplet's movement. The surfactants role here is to adhere to the fluid interface so that the surface tension is lowered, or adhere to the walls so that the wetting forces are reduced. In either case, reducing the capillary forces may enable the droplet's passage.

Our results showed that both methods could allow the droplet to enter the narrow capillary, although reducing the surface tension at the droplet's rear would initially make the droplet move backwards due to the Marangoni effect. Overall, we found that a surfactant which reduces the wetting forces is more efficient than one reducing the interfacial tension between the fluids.

### 5.1.4  Paper D

Paper D, "Non-ideal equation of state in the pseudo-potential lattice Boltzmann methods" was submitted to Physical Review E on April 13, 2010 and awaiting review.

The Shan-Chen model features diffuse interfaces, and for small droplets this can have an impact over the entire droplet, not just the interface. For small droplets and a small separation parameter, Laplace's law is not observed using the ideal gas equation. The separation forces create a non-ideal pressure, and it is usual to add a non-ideal term to the equation of state, but our experience is that the equation found in literature, which does not account for nearest neighbor interactions, is

imperfect. Paper D introduces an equation of state which accounts for the presence in neighboring sites.

Our results in the paper show that our proposed equation of state gives a considerably improved adherence to Laplace's law, particularly for simulations with highly diffuse interfaces. An immediate practical benefit is that using Laplace's law to determine the surface tension coefficient becomes more accurate.

## 5.2   Summary and outlook

The main focus of this thesis has been how to use the lattice-Boltzmann method to study surface tension and wetting, and in particular the effect a spatial variation in surface tension has on the flow. The spatial variation in these capillary effects is assumed to be due to the presence of a surfactant.

During my study, I have been in close cooperation with, and later employed by, the Centre for Integrated Petroleum Research. Therefore, the main application has been in the field of enhanced oil recovery. With several oil fields maturing, recovering the oil is of high economic interest.

In order to conduct studies of multiphase flows with variable surface tension, it was necessary to implement a means to track solute flow, and to program the effect the solute has on the surface tension.

In the thesis, it was assumed that surfactants are solute components which are attracted to areas where both oil and water are present, this made the surfactant flow towards the oil-water interface. The purpose of this is to mimic adsorption behavior. Since the the adsorption of surfactant particles to an interface is a physically complex process, it is likely that the simulation of surfactant movement may need to be altered to achieve greater physical accuracy. Our assumption that the surface tension decreases by an amount proportional to the concentration may also be challenged, but if another relationship between surfactant concentration and surface tension is established, it is easy to modify the program to accommodate this.

The simulations conducted in paper B showed that if the values for the surface tension coefficients *are* accurate, the simulated fluid flow due to the Marangoni effect is in good accordance with the flow predicted by theory.

The examples in the thesis have all used fairly simple geometries. Some simulations have been conducted on domains with no walls at all, with periodic boundary conditions at the edges. Others are in simple closed boxes or channels. This is justified by our need to keep simulations simple, and test the validity of our model by examining situations where some comparison to known results is possible.

However, if we want to simulate oil and water in a real reservoir, we need to take into account that these processes take place in porous media where the fluid-wall

boundaries are highly complex. The bounceback condition described in Section 2.5.1 can handle complex boundaries easily, and there exist several other means to implement boundaries if a more accurate simulation is required.

The simulator used in the thesis is limited by being two-dimensional. Realistic simulation of the porous medium, and the flow through it, requires an extension to three dimensions. At CIPR, work with a three-dimensional version of the method has started but is not a part of the thesis. Three-dimensional models are more complex than the two-dimensional ones, and require more computational effort.

The study of flows in complex porous media raises several questions. In the highly simplified tubes we used in paper C, we saw that when surfactant is applied to the rear of an oil droplet, the Marangoni effect caused the droplet to initially flow backwards. Eventually diffusion of the surfactant reduces the surface tension over the entire droplet. Whether this behavior is replicated in more complex media is less certain.

# Bibliography

[1] L. D. Landau and E. M. Lifshitz, *Fluid Mechanics*. Pergamon Press, 2nd ed., 1987.

[2] P.-G. de Gennes, F. Brochard-Wyart, and D. Quere, *Capillarity and Wetting Phenomena. Drops, Bubbles, Pearls, Waves*. Springer, 2004.

[3] T. F. Tadros, ed., *Emulsion Science and Technology*. Wiley-VCH, 2009.

[4] J. Bear, *Dynamics of fluids in porous media*. American Elsevier Publishing Company, 1972.

[5] R. J. M. DeWiest, *Flow through Porous Media*. Academic Press, 1969.

[6] P. G. de Gennes and C. Taupin, "Microemulsions and the Flexibility of Oil/Water Interfaces," *J. Phys. Chem.*, vol. 86, no. 2294–2304, 1982.

[7] S. G. Oh and D. O. Shah, "Effect of Counterions on the Interfacial Tension and Emulsion Droplet Size in the Oil/Water/Dodecyl Sulfate System," *J. Phys. Chem.*, vol. 97, pp. 284–286, 1993.

[8] K. Shinoda, T. Yamaguchi, and R. Hori, "The Surface Tension and the Critical Micelle Concentration in Aqueous Solution of $\beta$-D-Alkyl Glucosides and their Mixtures," *Bull. Chem. Soc. Jpn.*, vol. 34, no. 2, 1961.

[9] V. G. Levich and V. S. Krylov, "Surface-tension-driven Phenomena," *Ann. Rev. Fluid Mech.*, vol. 1, pp. 293–316, 1969.

[10] V. G. Levich and A. M. Kuznetzov, "Motion of drops in liquids under influence of surface-active substances," *Doklady Akademii Nauk SSSR*, vol. 146, no. 1, pp. 145–147, 1962.

[11] S. Thomas, "Enhanced Oil Recovery – An Overview," *Oil Gas Sci Technol*, vol. 63, no. 1, pp. 9–19, 2008.

[12] A. Gunstensen and D. Rothman, "Lattice-Boltzmann studies of immiscible two-phase flow through porous media," *J. Geophys. Res.*, vol. 98, no. B4, pp. 5431–6441, 1993.

[13] K. Langaas, *Modelling of Immiscible Two-Phase Flow in Porous Media with the Binary Fluid Lattice Boltzmann Method*. PhD thesis, Department of Physics, University of Bergen, 1999.

[14] K. Langaas and D. Grubert, "Lattice Boltzmann simulations of wetting and its application to disproportionate permeability reducing gel," *J. Petrol. Sci. Eng.*, vol. 24, no. 2–4, pp. 199–211, 1999.

[15] K. Langaas and S. Nilsson, "Pore-scale simulations of disproportionate permeability reducing gels," *J. Petrol. Sci. Eng.*, vol. 25, no. 3–4, pp. 167–186, 2000.

[16] S. Cobos, M. Carvalho, and V. Alvarado, "Flow of oil-water emulsions through a constricted capillary," *Int. J. Multiphase Flow*, vol. 35, pp. 507–515, 2009.

[17] A. Hiorth, K. Kaster, A. Lohne, O. K. Siqveland, H. Beland, N. H. Giske, and A. Stavland, "Microbial enhanced oil recovery-mechanism," in *International Symposium of the Society of Core Analysts (Calgary, Canada)*, September 2007.

[18] H. P. Greenspan, "On The Dynamics of Cell Cleavage," *J. theor. Biol.*, vol. 65, pp. 79–99, 1976.

[19] H. P. Greenspan, "On the Deformation of a Viscous Droplet Caused by Variable Surface Tension," *Stud. Appl. Math.*, vol. 57, no. 1, pp. 45–58, 1977.

[20] T. Sapir and A. Nir, "A Hydrodynamic Study of the Furrowing Stage During Cleavage," *PhysicoChem. Hydrodyn.*, vol. 6, pp. 803–814, 1985.

[21] Z. Li and S. R. Lubkin, "Numerical analysis of interfacial two-dimensional Stokes flow with discontinuous viscosity and variable surface tension," *Int. J. Numer. Meth. Fluids*, vol. 37, pp. 525–540, 2001.

[22] G. R. McNamara and G. Zanetti, "Use of the Boltzmann Equation to Simulate Lattice-Gas Automata," *Phys. Rev. Lett.*, vol. 61, no. 20, pp. 2332–2335, 1988.

[23] S. Succi, *The Lattice Boltzmann Equation for Fluid Mechanics and Beyond*. Oxford Sciene Publications, 2001.

[24] N. S. Martys and H. Chen, "Simulation of multicomponent fluids in complex three-dimensional geometries by the lattice Boltzmann method," *Phys. Rev. E*, vol. 53, no. 1, pp. 743–751, 1996.

[25] D. A. Wolf-Gladrow, *Lattice-Gas Cellular Automata and Lattice Boltzmann Models: An Introduction (Lecture Notes in Mathematics)*. Springer, 2000.

[26] J. Hardy, O. de Pazzis, and Y. Pomeau, "Time Evolution of a Two-Dimensional Classical Lattice System," *Phys. Rev. Lett.*, vol. 31, no. 5, pp. 276–279, 1973.

[27] J. Hardy, O. de Pazzis, and Y. Pomeau, "Time Evolution of a Two-Dimensional Classical Lattice System. I. Invariant states and time correlation functions," *J. Math. Phys.*, vol. 14, no. 12, pp. 1746–17599, 1973.

[28] J. Hardy, O. de Pazzis, and Y. Pomeau, "Molecular dynamics of a classical lattice gas: Transport properties and time correlation functions," *Phys. Rev. A*, vol. 13, no. 5, pp. 1949–1961, 1976.

[29] U. Frisch, B. Hasslacher, and Y. Pomeau, "Lattice-Gas Automata for the Navier-Stokes Equation," *Phys. Rev. Lett.*, vol. 56, no. 15, pp. 1505–1508, 1986.

[30] A. K. Gunstensen and D. H. Rothman, "A Galilean-invariant immiscible lattice gas ," *Physica D*, vol. 47, no. 1–2, pp. 53–63, 1991.

[31] D. D'Humieres, P. Lallemand, and U. Frisch, "Lattice Gas Models for 3D Hydrodynamics," *Europhys. Lett.*, vol. 2, no. 4, pp. 291–297, 1986.

[32] S. Wolfram, "Cellular Automaton Fluids 1: Basic Theory," *J. Stat. Phys.*, 1986.

[33] X. He and L.-S. Luo, "A priori derivation of the lattice Boltzmann equation," *Phys. Rev. E*, vol. 55, no. 6, pp. 6811–6817, 1996.

[34] X. He and L.-S. Luo, "Theory of the lattice Boltzmann method: From the Boltzmann equation to the lattice Boltzmann equation," *Phys. Rev. E*, pp. 6333–6336, 1997.

[35] J. M. Buick, *Lattice Boltzmann Methods in Interfacial Wave Modelling*. PhD thesis, The University of Edinburgh, 1997.

[36] S. Chapman and T. G. Cowling, *The Mathematical Theory of Non-Uniform Gases*. Cambridge University Press, 1970.

[37] P. L. Bhatnagar, E. P. Gross, and M. Krook, "A model for collision processes in gases. i. small amplitude processes in charged and neutral one-component systems," *Phys. Rev.*, vol. 94, pp. 511–525, May 1954.

[38] Y. Qian, D. D'Humieres, and P. Lallemand, "Lattice BGK Models for Navier-Stokes Equation," *Europhys. Lett.*, vol. 17, no. 6, pp. 479–484, 1992.

[39] D. D'Humieres, I. Ginzburg, M. Krafczyk, P. Lallemand, and L.-S. Luo, "Multiple-relaxation-time lattice Boltzmann models in three dimensions," *Phil. Trans. R. Soc. A*, vol. 360, pp. 437–451, 2002.

[40] L.-S. Luo, "Lecture 3. generalized lattice boltzmann equation." Lecture notes to short course at TU Braunschweig, pdf-file at http://research.nianet.org/~luo/Reprintsluo/Notes/TUBraunschweig_03/TUB03-3.pdf.

[41] S. Chen, D. Martinez, and R. Mei, "On boundary conditions in lattice Boltzmann methods," *Phys. Fluids*, vol. 8, pp. 2527–2536, September 1996.

[42] X. He, Q. Zou, L.-S. Luo, and M. Dembo, "Analytic Solutions of Simple Flows and Analysis of Nonslip Boundary Conditions for the Lattice Boltzmann BGK Model," *J. Stat. Phys.*, vol. 87, no. 1/2, pp. 115–136, 1997.

[43] D. R. Noble, S. Chen, J. G. Georgiadis, and R. O. Buckius, "A consistent hydrodynamic boundary condition for the lattice Boltzmann method," *Phys. Fluids*, vol. 7, no. 1, 1995.

[44] R. Maier and R. Bernard, "Lattice-Boltzmann accuracy in pore-scale flow simulation ," *J. Comp. Phys.*, vol. 229, no. 2, pp. 233–255, 2010.

[45] S. Chen and G. D. Doolen, "Lattice Boltzmann method for fluid flows," *Annu. Rev. Fluid Mech.*, vol. 30, pp. 329–364, 1998.

[46] Q. Zou and X. He, "On pressure and velocity boundary conditions for the lattice Boltzmann BGK model," *Phys. Fluids*, vol. 9, no. 6, pp. 1591–1598, 1997.

[47] X. He, L.-S. Luo, and M. Dembo, "Some progress in the lattice Boltzmann method: Reynolds number enhancement in simulations," *Physica A*, vol. 239, pp. 276–285, 1997.

[48] M. C. Sukop and D. T. Thorne, *Lattice Boltzmann Modeling, An Introduction for Geoscientists and Engineers*. Springer, 2006.

[49] C. Y. Lim, C. Shu, X. D. Niu, and Y. T. Chew, "Application of lattice Boltzmann metod to simulate microchannel flows," *Phys. Fluids*, vol. 14, no. 7, pp. 2209–2308, 2002.

[50] A. K. Gunstensen, D. H. Rothmann, S. Zaleski, and G. Zanetti, "Lattice Boltzmann model of immiscible fluids," *Phys. Rev. A*, vol. 43, no. 8, pp. 4320–4328, 1991.

[51] D. H. Rothman and J. M. Keller, "Immiscible Cellular-Automaton Fluids," *J. Stat. Phys.*, vol. 52, no. 3/4, pp. 1119–1127, 1988.

[52] T. Reis and T. N. Phillips, "Lattice Boltzmann model for simulating immiscible two-phase flows," *J. Phys. A. Math. Theor.*, vol. 40, pp. 4033–4053, 2007.

[53] L. Wu, M. Tsutahara, and S. Tajiri, "An Improved Lattice Boltzmann Model for Immiscible Fluids," *J. Comput. Sci. Technol.*, vol. 2, no. 2, pp. 307–317, 2008.

[54] J. Tölke, S. Freudinger, and M. Krafczyk, "An adaptive scheme using hierarchial grids for lattice Boltzmann multi-phase flow simulations," *Comput. Fluids*, vol. 35, pp. 820–830, 2006.

[55] J. Tölke, M. Krafczyk, M. Schulz, and E. Rank, "Lattice Boltzmann simulations of binary fluid flow through porous media," *Phil. Trans. R. Soc. A*, vol. 360, pp. 535–545, 2002.

[56] D. Grunau, S. Chen, and K. Eggert, "A lattice Boltzmann model for multiphase fluid flows," *Phys. Fluids A*, vol. 5, no. 10, pp. 2557–2562, 1993.

[57] M. Latva-Kokko and D. H. Rothman, "Diffusion properties of gradient-based lattice Boltzmann models of immiscible fluids," *Phys. Rev. E*, vol. 71, p. 056802, 2005.

[58] U. D'Ortona, D. Salin, M. Cieplak, R. B. Rybka, and J. R. Banavar, "Two-color nonlinear Boltzmann cellular automata: Surface tension and wetting," *Phys. Rev. E*, vol. 51, no. 4, pp. 3718–3728, 1995.

[59] M. Latva-Kokko and D. H. Rothman, "Static contact angle in lattice Boltzmann models of immiscible fluids," *Phys. Rev. E*, vol. 72, p. 046701, 2005.

[60] X. Shan and H. Chen, "Lattice Boltzmann model for simulating flows with multiple phases and components," *Phys. Rev. E*, vol. 47, pp. 1815–1820, March 1993.

[61] X. Shan and H. Chen, "Simulation of nonideal gases and liquid-gas phase transitions by the lattice Boltzmann equation," *Phys. Rev. E*, vol. 49, pp. 2941–2948, April 1994.

[62] M. Sbragaglia, R. Benzi, L. Biferale, S. Succi, K. Sugiyama, and F. Toschi, "Generalized lattice Boltzmann method with multirange pseudopotential," *Phys. Rev. E*, vol. 75, p. 026702, 2007.

[63] L. C. Evans, *Partial Differential Equations*. American Mathematical Society, 2000.

[64] P. Yuan and L. Schaeffer, "Equations of state in a lattice Boltzmann model," *Phys. Fluids*, vol. 18, p. 042101, 2006.

[65] X. He and G. D. Doolen, "Thermodynamic Foundations of Kinetic Theory and Lattice Boltzmann Models for Multiphase Flows," *J. Stat. Phys*, vol. 107, no. 1/2, pp. 309–328, 2002.

[66] X. Shan, "Pressure tensor calculation in a class of nonideal gas lattice Boltzmann models," *Phys. Rev. E*, vol. 77, p. 066702, 2008.

[67] N. S. Martys and J. F. Douglas, "Critical properties and phase separation in lattice Boltzmann fluid mixtures," *Phys. Rev. E*, vol. 63, p. 031205, 2001.

[68] R. Benzi, L. Biferale, M. Sbragaglia, S. Succi, and F. Toschi, "Mesoscopic modeling of a two-phase flow in the presence of boundaries: The contact angle," *Phys. Rev. E*, vol. 74, p. 021509, 2006.

[69] Q. Kang, D. Zhang, and S. Chen, "Displacement of a two-dimensional immiscible droplet in a channel," *Phys. Fluids*, vol. 14, no. 9, pp. 3203–3214, 2002.

[70] H. Huang, D. T. Thorne, M. G. Schaap, and M. C. Sukop, "Proposed approximation for contact angles in Shan-and-Chen-type multicomponent multiphase lattice Boltzmann models," *Phys. Rev. E*, vol. 76, 2007. 066701.

[71] M. G. Schaap, M. L. Porter, B. S. B. Christensen, and D. Wildenschild, "Comparison of pressure-saturation characteristics derived from computed tomography and lattice Boltzmann simulations," *Water Resour. Res.*, vol. 43, p. W12S06, 2007.

[72] E. Orlandini, M. Swift, and J. Yeomans, "A Lattice Boltzmann Model of Binary-Fluid Mixtures," *Europhys. Lett.*, vol. 32, no. 6, pp. 463–468, 1995.

[73] M. R. Swift, W. Osborn, and J. Yeomans, "Lattice Boltzmann Simulation of Nonideal Fluids," *Phys. Rev. Lett.*, vol. 75, no. 5, pp. 830–834, 1995.

[74] M. R. Swift, E. Orlandini, W. Osborn, and J. Yeomans, "Lattice Boltzmann simulations of liquid-gas and binary fluid systems," *Phys. Rev. E*, vol. 54, no. 5, pp. 5041–5052, 1996.

[75] J. Chin, E. S. Boek, and P. V. Coveney, "Lattice Boltzmann simulation of the flow of binary immiscible fluids with different viscosities using the Shan-Chen microscopic interaction model," *Phil. Trans. R. Soc. A*, vol. 360, pp. 547–548, 2002.

[76] R. R. Nourgaliev, T. N. Dinh, T. G. Theofanous, and D. Joseph, "The lattice Boltzmann equation method: theoretical interpretation, numerics and implications," *Internat. J. Multiphase Flow*, vol. 29, no. 1, pp. 117–169, 2003.

[77] J. M. Yeomans, "Mesoscale simulations: Lattice Boltzmann and particle algorithms," *Physica A*, vol. 369, pp. 159–184, 2006.

[78] L.-S. Luo, "Unified Theory of Lattice Boltzmann Models for Nonideal Gases," *Phys. Rev. Lett.*, vol. 81, no. 8, pp. 1618–1621, 1998.

[79] L.-S. Luo and S. S. Girimaji, "Lattice Boltzmann model for binary mixtures," *Phys. Rev. E*, vol. 66, p. 035301, 2002.

[80] L.-S. Luo and S. S. Girimaji, "Theory of the lattice Boltzmann method: Two fluid model for binary mixtures," *Phys. Rev. E*, vol. 67, p. 036302, 2003.

[81] Z. Guo and T. Zhao, "Discrete velocity and lattice Boltzmann models for binary mixtures of nonideal fluids," *Phys. Rev. E*, vol. 68, p. 035302(R), 2003.

[82] Z. Guo and T. Zhao, "Finite-difference-based lattice Boltzmann model for dense binary mixtures," *Phys. Rev. E*, vol. 71, p. 026701, 2005.

[83] P. Lallemand, L.-S. Luo, and Y. Peng, "A lattice Boltzmann front-tracking method for interface dynamics with surface tension in two dimensions," *J. Comp. Phys.*, vol. 226, pp. 1367–1384, 2007.

[84] Q. Kang, D. Zhang, S. Chen, and X. He, "Lattice Boltzmann simulation of chemical dissolution in porous media," *Phys. Rev. E*, vol. 65, 2002.

[85] S. P. Dawson, S. Chen, and G. Doolen, "Lattice Boltzmann computations for reaction-diffusion equations," *J. Chem. Phys.*, vol. 98, no. 2, pp. 1514–1523, 1993.

[86] G. Gonnella, E. Orlandini, and J. M. Yeomans, "Lattice Boltzmann simulations of lamellar and droplet phases," *Phys. Rev. E*, vol. 58, no. 1, pp. 480–485, 1998.

[87] O. Theissen, G. Gompper, and D. Kroll, "Lattice.Boltzmann model of amphiphilic systems," *Europhys. Lett.*, vol. 42, no. 4, pp. 419–424, 1998.

[88] A. Lamura and G. Gonnella, "Modeling the Dynamics of amphiphilic fluids," *Internat. J. Modern Phys. C*, vol. 9, no. 8, pp. 1469–1478, 1998.

[89] A. Lamura, G. Gonnella, and J. Yeomans, "A lattice Boltzmann model of ternary fluid mixtures," *Europhys. Lett.*, vol. 45, no. 3, pp. 314–320, 1999.

[90] H. Chen, B. M. Boghosian, P. V. Coveney, and M. Nekovee, "A Ternary Lattice Boltzmann Model for Amphiphile Fluids," *Proceedings: Mathematical, Physical and Engineering Sciences*, vol. 456, no. 2000, pp. 2043–2057, 2000.

[91] M. Nekovee, P. V. Coveney, H. Chen, and B. M. Boghosian, "Lattice-Boltzmann model for interacting amphiphilic fluids," *Phys. Rev. E*, vol. 62, no. 6, pp. 8282–8294, 2000.

[92] P. J. Love, M. Nekovee, P. V. Coveney, J. Chin, N. Gonzalez-Segredo, and J. M. R. Martin, "Simulations of amphiphilic fluids using mesoscale lattice-Boltzmann and lattice-gas methods," *Comput. Phys. Comm.*, vol. 153, no. 3, pp. 340–358, 2003.